

Measurement of K_S^0 , Λ and $\bar{\Lambda}$ production at HERA

ZEUS Collaboration

Abstract

The production of the neutral strange hadrons K_S^0 , Λ and $\bar{\Lambda}$ has been measured in ep collisions at HERA using the ZEUS detector. Cross sections, baryon-to-meson ratios, relative yields of strange and charged light hadrons, Λ ($\bar{\Lambda}$) asymmetry and polarization have been measured in three kinematic regions: $Q^2 > 25 \text{ GeV}^2$; $5 < Q^2 < 25 \text{ GeV}^2$; and in photoproduction ($Q^2 \simeq 0$). In photoproduction the presence of two hadronic jets, each with at least 5 GeV transverse energy, was required. The measurements agree in general with Monte Carlo models and are consistent with measurements made at e^+e^- colliders, except for an enhancement of baryon relative to meson production in photoproduction.

The ZEUS Collaboration

S. Chekanov¹, M. Derrick, S. Magill, S. Miglioranzi², B. Musgrave, D. Nicholass², J. Repond, R. Yoshida

*Argonne National Laboratory, Argonne, Illinois 60439-4815, USA*ⁿ

M.C.K. Mattingly

Andrews University, Berrien Springs, Michigan 49104-0380, USA

M. Jechow, N. Pavel[†], A.G. Yagües Molina

Institut für Physik der Humboldt-Universität zu Berlin, Berlin, Germany

S. Antonelli, P. Antonioli, G. Bari, M. Basile, L. Bellagamba, M. Bindi, D. Boscherini, A. Bruni, G. Bruni, L. Cifarelli, F. Cindolo, A. Contin, M. Corradi³, S. De Pasquale, G. Iacobucci, A. Margotti, R. Nania, A. Polini, L. Rinaldi, G. Sartorelli, A. Zichichi

University and INFN Bologna, Bologna, Italy^e

D. Bartsch, I. Brock, S. Goers⁴, H. Hartmann, E. Hilger, H.-P. Jakob, M. Jünger, O.M. Kind, E. Paul⁵, J. Rautenberg⁶, R. Renner, U. Samson, V. Schönberg, R. Shehzadi, M. Wang⁷, M. Wlasenko

Physikalisches Institut der Universität Bonn, Bonn, Germany^b

N.H. Brook, G.P. Heath, J.D. Morris, T. Namsoo

H.H. Wills Physics Laboratory, University of Bristol, Bristol, United Kingdom^m

M. Capua, S. Fazio, A. Mastroberardino, M. Schioppa, G. Susinno, E. Tassi

Calabria University, Physics Department and INFN, Cosenza, Italy^e

J.Y. Kim⁸, K.J. Ma⁹

Chonnam National University, Kwangju, South Korea^g

Z.A. Ibrahim, B. Kamaluddin, W.A.T. Wan Abdullah

Jabatan Fizik, Universiti Malaya, 50603 Kuala Lumpur, Malaysia^r

Y. Ning, Z. Ren, F. Sciulli

Nevis Laboratories, Columbia University, Irvington on Hudson, New York 10027^o

J. Chwastowski, A. Eskreys, J. Figiel, A. Galas, M. Gil, K. Olkiewicz, P. Stopa, L. Zawiejski

*The Henryk Niewodniczanski Institute of Nuclear Physics, Polish Academy of Sciences, Cracow, Poland*ⁱ

L. Adamczyk, T. Bołd, I. Grabowska-Bołd, D. Kisielewska, J. Łukasik, M. Przybycień, L. Suszycki

Faculty of Physics and Applied Computer Science, AGH-University of Science and Technology, Cracow, Poland^p

A. Kotański¹⁰, W. Słomiński

Department of Physics, Jagellonian University, Cracow, Poland

V. Adler, U. Behrens, I. Bloch, A. Bonato, K. Borrás, N. Coppola, J. Fourletova, A. Geiser, D. Gladkov, P. Göttlicher¹¹, I. Gregor, T. Haas, W. Hain, C. Horn, B. Kahle, U. Kötz, H. Kowalski, E. Lobodzinska, B. Lühr, R. Mankel, I.-A. Melzer-Pellmann, A. Montanari, D. Notz, A.E. Nuncio-Quiroz, R. Santamarta, U. Schneekloth, A. Spiridonov¹², H. Stadie, U. Stösslein, D. Szuba¹³, J. Szuba¹⁴, T. Theedt, G. Wolf, K. Wrona, C. Youngman, W. Zeuner

Deutsches Elektronen-Synchrotron DESY, Hamburg, Germany

W. Lohmann, S. Schlenstedt

Deutsches Elektronen-Synchrotron DESY, Zeuthen, Germany

G. Barbagli, E. Gallo, P. G. Pelfer

University and INFN, Florence, Italy^e

A. Bamberger, D. Dobur, F. Karstens, N.N. Vlasov¹⁵

Fakultät für Physik der Universität Freiburg i.Br., Freiburg i.Br., Germany^b

P.J. Bussey, A.T. Doyle, W. Dunne, J. Ferrando, D.H. Saxon, I.O. Skillicorn

Department of Physics and Astronomy, University of Glasgow, Glasgow, United Kingdom^m

I. Gialas¹⁶

Department of Engineering in Management and Finance, Univ. of Aegean, Greece

T. Gosau, U. Holm, R. Klanner, E. Lohrmann, H. Salehi, P. Schleper, T. Schörner-Sadenius, J. Sztuk, K. Wichmann, K. Wick

Hamburg University, Institute of Exp. Physics, Hamburg, Germany^b

C. Foudas, C. Fry, K.R. Long, A.D. Tapper

Imperial College London, High Energy Nuclear Physics Group, London, United Kingdom^m

M. Kataoka¹⁷, T. Matsumoto, K. Nagano, K. Tokushuku¹⁸, S. Yamada, Y. Yamazaki

Institute of Particle and Nuclear Studies, KEK, Tsukuba, Japan^f

A.N. Barakbaev, E.G. Boos, A. Dossanov, N.S. Pokrovskiy, B.O. Zhautykov

Institute of Physics and Technology of Ministry of Education and Science of Kazakhstan, Almaty, Kazakhstan

D. Son

Kyungpook National University, Center for High Energy Physics, Daegu, South Korea^g

J. de Favereau, K. Piotrkowski

Institut de Physique Nucléaire, Université Catholique de Louvain, Louvain-la-Neuve, Belgium^g

F. Barreiro, C. Glasman¹⁹, M. Jimenez, L. Labarga, J. del Peso, E. Ron, M. Soares, J. Terrón, M. Zambrana

Departamento de Física Teórica, Universidad Autónoma de Madrid, Madrid, Spain^l

F. Corriveau, C. Liu, R. Walsh, C. Zhou

Department of Physics, McGill University, Montréal, Québec, Canada H3A 2T8^a

T. Tsurugai

Meiji Gakuin University, Faculty of General Education, Yokohama, Japan^f

A. Antonov, B.A. Dolgoshein, I. Rubinsky, V. Sosnovtsev, A. Stifutkin, S. Suchkov

Moscow Engineering Physics Institute, Moscow, Russia^j

R.K. Dementiev, P.F. Ermolov, L.K. Gladilin, I.I. Katkov, L.A. Khein, I.A. Korzhavina, V.A. Kuzmin, B.B. Levchenko²⁰, O.Yu. Lukina, A.S. Proskuryakov, L.M. Shcheglova, D.S. Zotkin, S.A. Zotkin

Moscow State University, Institute of Nuclear Physics, Moscow, Russia^k

I. Abt, C. Büttner, A. Caldwell, D. Kollar, W.B. Schmidke, J. Sutiak

Max-Planck-Institut für Physik, München, Germany

G. Grigorescu, A. Keramidas, E. Koffeman, P. Kooijman, A. Pellegrino, H. Tiecke, M. Vázquez¹⁷, L. Wiggers

NIKHEF and University of Amsterdam, Amsterdam, Netherlands^h

N. Brümmer, B. Bylsma, L.S. Durkin, A. Lee, T.Y. Ling

Physics Department, Ohio State University, Columbus, Ohio 43210ⁿ

P.D. Allfrey, M.A. Bell, A.M. Cooper-Sarkar, A. Cottrell, R.C.E. Devenish, B. Foster, K. Korcsak-Gorzo, S. Patel, V. Roberfroid²¹, A. Robertson, P.B. Straub, C. Uribe-Estrada, R. Walczak

Department of Physics, University of Oxford, Oxford United Kingdom^m

P. Bellan, A. Bertolin, R. Brugnera, R. Carlin, R. Ciesielski, F. Dal Corso, S. Dusini, A. Garfagnini, S. Limentani, A. Longhin, L. Stanco, M. Turcato

Dipartimento di Fisica dell' Università and INFN, Padova, Italy^e

B.Y. Oh, A. Raval, J. Ukleja²², J.J. Whitmore²³

Department of Physics, Pennsylvania State University, University Park, Pennsylvania 16802^o

Y. Iga

Polytechnic University, Sagamihara, Japan^f

G. D'Agostini, G. Marini, A. Nigro
Dipartimento di Fisica, Università 'La Sapienza' and INFN, Rome, Italy^e

J.E. Cole, J.C. Hart
Rutherford Appleton Laboratory, Chilton, Didcot, Oxon, United Kingdom^m

H. Abramowicz²⁴, A. Gabareen, R. Ingbir, S. Kananov, A. Levy
Raymond and Beverly Sackler Faculty of Exact Sciences, School of Physics, Tel-Aviv University, Tel-Aviv, Israel^d

M. Kuze
Department of Physics, Tokyo Institute of Technology, Tokyo, Japan^f

R. Hori, S. Kagawa²⁵, N. Okazaki, S. Shimizu, T. Tawara
Department of Physics, University of Tokyo, Tokyo, Japan^f

R. Hamatsu, H. Kaji²⁶, S. Kitamura²⁷, O. Ota, Y.D. Ri
Tokyo Metropolitan University, Department of Physics, Tokyo, Japan^f

M.I. Ferrero, V. Monaco, R. Sacchi, A. Solano
Università di Torino and INFN, Torino, Italy^e

M. Arneodo, M. Ruspa
Università del Piemonte Orientale, Novara, and INFN, Torino, Italy^e

S. Fourletov, J.F. Martin
Department of Physics, University of Toronto, Toronto, Ontario, Canada M5S 1A7^a

S.K. Boutle¹⁶, J.M. Butterworth, C. Gwenlan²⁸, T.W. Jones, J.H. Loizides, M.R. Sutton²⁸,
 C. Targett-Adams, M. Wing
Physics and Astronomy Department, University College London, London, United Kingdom^m

B. Brzozowska, J. Ciborowski²⁹, G. Grzelak, P. Kulinski, P. Luźniak³⁰, J. Malka³⁰, R.J. Nowak,
 J.M. Pawlak, T. Tymieniecka, A. Ukleja³¹, A.F. Żarnecki
Warsaw University, Institute of Experimental Physics, Warsaw, Poland

M. Adamus, P. Plucinski³²
Institute for Nuclear Studies, Warsaw, Poland

Y. Eisenberg, I. Giller, D. Hochman, U. Karshon, M. Rosin
Department of Particle Physics, Weizmann Institute, Rehovot, Israel^c

E. Brownson, T. Danielson, A. Everett, D. Kçira, D.D. Reeder, P. Ryan, A.A. Savin,
 W.H. Smith, H. Wolfe
Department of Physics, University of Wisconsin, Madison, Wisconsin 53706, USAⁿ

S. Bhadra, C.D. Catterall, Y. Cui, G. Hartner, S. Menary, U. Noor, J. Standage, J. Whyte
Department of Physics, York University, Ontario, Canada M3J 1P3^a

- ¹ supported by DESY, Germany
- ² also affiliated with University College London, UK
- ³ also at University of Hamburg, Germany, Alexander von Humboldt Fellow
- ⁴ self-employed
- ⁵ retired
- ⁶ now at Univ. of Wuppertal, Germany
- ⁷ now at University of Regina, Canada
- ⁸ supported by Chonnam National University in 2005
- ⁹ supported by a scholarship of the World Laboratory Björn Wiik Research Project
- ¹⁰ supported by the research grant no. 1 P03B 04529 (2005-2008)
- ¹¹ now at DESY group FEB, Hamburg, Germany
- ¹² also at Institut of Theoretical and Experimental Physics, Moscow, Russia
- ¹³ also at INP, Cracow, Poland
- ¹⁴ on leave of absence from FPACS, AGH-UST, Cracow, Poland
- ¹⁵ partly supported by Moscow State University, Russia
- ¹⁶ also affiliated with DESY
- ¹⁷ now at CERN, Geneva, Switzerland
- ¹⁸ also at University of Tokyo, Japan
- ¹⁹ Ramón y Cajal Fellow
- ²⁰ partly supported by Russian Foundation for Basic Research grant no. 05-02-39028-NSFC-a
- ²¹ EU Marie Curie Fellow
- ²² partially supported by Warsaw University, Poland
- ²³ This material was based on work supported by the National Science Foundation, while working at the Foundation.
- ²⁴ also at Max Planck Institute, Munich, Germany, Alexander von Humboldt Research Award
- ²⁵ now at KEK, Tsukuba, Japan
- ²⁶ now at Nagoya University, Japan
- ²⁷ Department of Radiological Science
- ²⁸ PPARC Advanced fellow
- ²⁹ also at Łódź University, Poland
- ³⁰ Łódź University, Poland
- ³¹ supported by the Polish Ministry for Education and Science grant no. 1 P03B 12629
- ³² supported by the Polish Ministry for Education and Science grant no. 1 P03B 14129

† deceased

- ^a supported by the Natural Sciences and Engineering Research Council of Canada (NSERC)
- ^b supported by the German Federal Ministry for Education and Research (BMBF), under contract numbers HZ1GUA 2, HZ1GUB 0, HZ1PDA 5, HZ1VFA 5
- ^c supported in part by the MINERVA Gesellschaft für Forschung GmbH, the Israel Science Foundation (grant no. 293/02-11.2) and the U.S.-Israel Binational Science Foundation
- ^d supported by the German-Israeli Foundation and the Israel Science Foundation
- ^e supported by the Italian National Institute for Nuclear Physics (INFN)
- ^f supported by the Japanese Ministry of Education, Culture, Sports, Science and Technology (MEXT) and its grants for Scientific Research
- ^g supported by the Korean Ministry of Education and Korea Science and Engineering Foundation
- ^h supported by the Netherlands Foundation for Research on Matter (FOM)
- ⁱ supported by the Polish State Committee for Scientific Research, grant no. 620/E-77/SPB/DESY/P-03/DZ 117/2003-2005 and grant no. 1P03B07427/2004-2006
- ^j partially supported by the German Federal Ministry for Education and Research (BMBF)
- ^k supported by RF Presidential grant N 1685.2003.2 for the leading scientific schools and by the Russian Ministry of Education and Science through its grant for Scientific Research on High Energy Physics
- ^l supported by the Spanish Ministry of Education and Science through funds provided by CICYT
- ^m supported by the Particle Physics and Astronomy Research Council, UK
- ⁿ supported by the US Department of Energy
- ^o supported by the US National Science Foundation. Any opinion, findings and conclusions or recommendations expressed in this material are those of the authors and do not necessarily reflect the views of the National Science Foundation.
- ^p supported by the Polish Ministry of Science and Higher Education
- ^q supported by FNRS and its associated funds (IISN and FRiA) and by an Inter-University Attraction Poles Programme subsidised by the Belgian Federal Science Policy Office
- ^r supported by the Malaysian Ministry of Science, Technology and Innovation/Akademi Sains Malaysia grant SAGA 66-02-03-0048

1 Introduction

Production of K_S^0 , Λ and $\bar{\Lambda}$ hadrons has been extensively studied at particle colliders: e^+e^- [1–3], ep [4], $p\bar{p}$ [5, 6] and pp [7]. The data have been used to test QCD and build phenomenological models extending QCD predictions beyond what can be calculated from first principles.

The results on K_S^0 , Λ , and $\bar{\Lambda}$ production presented in this paper are based on a data sample of 121 pb^{-1} collected by the ZEUS experiment at HERA, about 100 times larger than used in previous HERA publications [4] and extend the kinematical region of the measurements, thereby providing a tighter constraint on models.

The measurements have been performed in three different regions of Q^2 , where Q^2 is the virtuality of the exchanged boson: Deep Inelastic Scattering (DIS) with $Q^2 > 25 \text{ GeV}^2$; DIS with $5 < Q^2 < 25 \text{ GeV}^2$; and photoproduction, $Q^2 \simeq 0 \text{ GeV}^2$, in which a quasi-real photon interacts with the proton. In the photoproduction sample, two jets, each of at least 5 GeV transverse energy, were required.

The following measurements are presented in this paper: differential cross sections, baryon-antibaryon asymmetry, baryon-to-meson ratio, ratio of strange-to-light hadrons, and the Λ and $\bar{\Lambda}$ transverse spin polarization. There was no attempt to separate direct production from resonance decays: all sources for K_S^0 , Λ , and $\bar{\Lambda}$ production were included. These measurements are relevant for modeling production of hadrons at high energies, for example in Monte Carlo (MC) programs [8–12], and for testing the mechanism for baryon transport along the rapidity axis [13], the mechanisms for baryon production [14], effects due to QCD instantons [15–17] and the mechanisms for the transverse spin polarization of hadrons [18–20].

2 Experimental setup

The data were collected by the ZEUS detector at the HERA ep collider during the running period 1996–2000. The data correspond to an integrated luminosity of 121 pb^{-1} , of which 82 pb^{-1} were collected at $\sqrt{s} = 318 \text{ GeV}$ (the electron or positron¹ beam energy, E_e^{beam} , was 27.5 GeV and the proton beam energy was 920 GeV) and 39 pb^{-1} at $\sqrt{s} = 300 \text{ GeV}$ (where the proton beam energy was 820 GeV).

A detailed description of the ZEUS detector can be found elsewhere [21]. A brief outline of the components that are most relevant for this analysis is given below.

¹ In the text, electron beam, as well as scattered electron, apply to both electron and positron.

Charged particles are tracked in the central tracking detector (CTD) [22], which operates in a magnetic field of 1.43 T provided by a thin superconducting coil. The CTD consists of 72 cylindrical drift chamber layers, organized in 9 superlayers covering the polar-angle² region $15^\circ < \theta < 164^\circ$. The transverse-momentum resolution for full-length tracks is $\sigma(p_T)/p_T = 0.0058p_T \oplus 0.0065 \oplus 0.0014/p_T$, with p_T in GeV.

The high-resolution uranium–scintillator calorimeter (CAL) [23] consists of three parts: the forward (FCAL), the barrel (BCAL) and the rear (RCAL) calorimeters. Each part is subdivided transversely into towers and longitudinally into one electromagnetic section and either one (in RCAL) or two (in BCAL and FCAL) hadronic sections. The smallest subdivision of the calorimeter is called a cell. The CAL energy resolutions, as measured under test-beam conditions, are $\sigma(E)/E = 0.18/\sqrt{E}$ for electrons and $\sigma(E)/E = 0.35/\sqrt{E}$ for hadrons, with E in GeV.

A three-level trigger system was used to select events on-line [21]. At the third level, DIS events were accepted on the basis of the identification of a scattered electron candidate using localised energy deposition in the CAL. As there was no possibility to select inclusive photoproduction sample, the requirement for photoproduction events [24] was based on running a jet algorithm using the energies and positions of the CAL cells. Events with at least two jets were accepted, where each jet was required to have transverse energy greater than 4.5 GeV and pseudorapidity³ less than 2.5.

The luminosity was measured using the bremsstrahlung process $ep \rightarrow ep\gamma$ with the luminosity monitor [25], a lead-scintillator calorimeter placed in the HERA tunnel at $Z = -107$ m.

3 Event reconstruction and selection

3.1 Deep inelastic scattering sample

The DIS events are characterised by a scattered electron detected in the CAL. The scattered electron was identified from the energy deposit in the CAL using a neural network [26]. The Bjorken variable x_{Bj} [27] and Q^2 were reconstructed using the double angle method (DA) [28] which has the best resolution in the Q^2 region studied. The inelasticity variable, y , was reconstructed using both the electron (e) [28] and Jacquet-

² The ZEUS coordinate system is a right-handed Cartesian system, with the Z axis pointing in the proton beam direction, referred to as the “forward direction”, and the X axis pointing left towards the center of HERA. The coordinate origin is at the nominal interaction point.

³ The pseudorapidity η is defined as $\eta \equiv -\ln \tan(\theta/2)$, where θ is a scattering angle.

Blondel (JB) [29] methods. The following requirements were applied offline to select events with $Q^2 > 25 \text{ GeV}^2$ (called the high- Q^2 sample):

- $|Z_{\text{vtx}}| < 50 \text{ cm}$ to reduce the background from non- ep collisions;
- $38 < \delta < 65 \text{ GeV}$, where $\delta = \sum_i (E_i - P_{Z,i})$ and the sum runs over the energy and longitudinal momentum of all CAL cell deposits. This cut reduced the background from photoproduction and events with large radiative corrections;
- an identified scattered electron with energy above 10 GeV ;
- the impact position of the scattered electron on the CAL satisfied $\sqrt{X^2 + Y^2} > 36 \text{ cm}$;
- the electron was isolated: the energy from all CAL cell deposits not associated with the scattered electron but in an $\eta - \phi$ cone of radius 0.8 centered on the electron was required to be below 5 GeV . This requirement reduced photoproduction background;
- a track match with any electron falling in the range $0.3 < \theta < 2.6$, well within the CTD acceptance. For θ outside this region, $\delta > 44 \text{ GeV}$ was required. This cut further suppressed events from non- ep interaction and photoproduction;
- $y_{\text{JB}} > 0.02$ to improve the accuracy of the DA reconstruction;
- $y_e < 0.95$ to remove events where fake electrons were found in the FCAL;
- $Q_{\text{DA}}^2 > 25 \text{ GeV}^2$.

The same selection was used to obtain the low- Q^2 DIS sample, except for the Q^2 requirement and the position of the scattered electron, which were as follows:

- the impact position of the scattered electron on the CAL was required to be outside a rectangle of dimensions $26 \times 14 \text{ cm}^2$, centred on the beam pipe;
- $5 < Q_{\text{DA}}^2 < 25 \text{ GeV}^2$.

The trigger for selecting low- Q^2 events was normally prescaled, so the data correspond to an integrated luminosity of 16.6 pb^{-1} .

It should be noted that there was no jet requirement in the DIS event samples.

3.2 Photoproduction sample

Photoproduction events were selected applying the following criteria, described in an earlier publication [24]:

- $|Z_{\text{vtx}}| < 50 \text{ cm}$, to reduce background from non- ep collisions;
- $y_{\text{JB}} > 0.2$, to further reduce background from non- ep collisions;

- events were removed where an electron was found with $y_e < 0.85$, reducing the background from neutral current DIS events;
- $y_{\text{JB}} < 0.85$, to reduce background from neutral current DIS events where the electron was not identified;
- charged current DIS events were removed by rejecting events with $P_T^{\text{miss}}/\sqrt{E_T} > 2.0 \text{ GeV}^{\frac{1}{2}}$, where P_T^{miss} is the missing transverse momentum and E_T is the total transverse energy.

Energy Flow Objects, reconstructed from a combination of calorimeter and tracking information to give the best resolution of kinematic variables, were used as the input to the k_T cluster jet-finding algorithm [30], which was run in the longitudinally invariant inclusive mode [31]. The transverse energy of the jets was corrected for energy losses in inactive material in front of the CAL, as described in a previous publication [32]. An event was accepted if it contained at least two jets, both satisfying the following criteria:

- jet transverse energy $E_T^{\text{jet}} > 5 \text{ GeV}$;
- jet pseudorapidity $|\eta^{\text{jet}}| < 2.4$.

Photoproduction events selected in this way contributed about 10% to the total photoproduction cross section. The photoproduction sample was divided into subsamples using the variable x_γ^{OBS} , a measure of the fraction of the photon energy transferred to the dijet system, defined as:

$$x_\gamma^{\text{OBS}} = \frac{\sum E_T^{\text{jet}} e^{-\eta^{\text{jet}}}}{2y_{\text{JB}} E_e^{\text{beam}}}$$

where the sum runs over the two jets with highest transverse energy. In leading-order QCD, $x_\gamma^{\text{OBS}} = 1$ corresponds to direct photon processes in which the photon takes part in the hard scattering as a point-like particle. Resolved photon processes, in which the photon acts as a source of partons, populate the region at $x_\gamma^{\text{OBS}} < 1$. The sample with $x_\gamma^{\text{OBS}} > 0.75$ is classified as direct-enriched, and that with $x_\gamma^{\text{OBS}} < 0.75$ as resolved-enriched.

3.3 Strange particle reconstruction

Candidates for long-lived neutral strange hadrons decaying to two charged particles were identified by selecting pairs of oppositely charged tracks, fitted to a displaced secondary vertex. Events were required to have at least one such candidate. These secondary vertices were found by the ZEUS track-finding software, which is based on minimizing the χ^2 arising from fitting tracks to vertices [33]. Displaced vertices were typically more than 3 cm away from the primary vertex. The minimal distance required to resolve a

displaced vertex from the primary vertex was about 1 cm. The tracks fitted to this vertex were required to pass through at least the fifth superlayer of the CTD, the transverse momentum was required to be greater than 150 MeV and the absolute pseudorapidity in the laboratory frame was required to be less than 1.5. These constraints ensured a good track resolution and acceptance. The Λ , $\bar{\Lambda}$ and K_S^0 particles may also be created in interactions with the beam pipe. To remove these events a collinearity cut on the angle between the reconstructed candidate momentum and the vector joining the primary vertex to secondary vertex was applied. This angle was restricted to be less than 0.2.

The $\Lambda(\bar{\Lambda})$ candidates were reconstructed by their charged decay mode to $p\pi^-$ ($\bar{p}\pi^+$) (branching ratio $63.9 \pm 0.5\%$ [34]). The track with the larger momentum was assigned the mass of the proton, while the other was assigned the mass of the charged pion, as the decay proton always has a larger momentum than the pion, provided the $\Lambda(\bar{\Lambda})$ momentum is greater than 0.3 GeV. Additional requirements to select $\Lambda(\bar{\Lambda})$ are given in the following:

- $0.6 < P_T^{\text{LAB}}(\Lambda, \bar{\Lambda}) < 2.5$ GeV, where $P_T^{\text{LAB}}(\Lambda, \bar{\Lambda})$ is the transverse momentum of the reconstructed candidate;
- $|\eta^{\text{LAB}}(\Lambda, \bar{\Lambda})| < 1.2$, where $\eta^{\text{LAB}}(\Lambda, \bar{\Lambda})$ is the pseudorapidity of the reconstructed candidate in the laboratory;
- $M(e^+e^-) > 0.05$ GeV, to eliminate electron pairs from photon conversions ⁴;
- $M(\pi^+\pi^-) < 0.475$ GeV, to remove K_S^0 contamination;
- $1.11 < M(p\pi) < 1.122$ GeV.

The K_S^0 meson candidates were reconstructed from the decays to $\pi^+\pi^-$ (branching ratio $68.95 \pm 0.14\%$ [34]). Both tracks were assigned the mass of the charged pion. Additional requirements to select K_S^0 are given in the following:

- $0.6 < P_T^{\text{LAB}}(K_S^0) < 2.5$ GeV, where $P_T^{\text{LAB}}(K_S^0)$ is the transverse momentum of the reconstructed candidate;
- $|\eta^{\text{LAB}}(K_S^0)| < 1.2$, where $\eta^{\text{LAB}}(K_S^0)$ is the pseudorapidity of the reconstructed candidate in the laboratory;
- $M(e^+e^-) > 0.05$ GeV;
- $M(p\pi) > 1.125$ GeV, to remove Λ and $\bar{\Lambda}$ contamination. Here the mass of the proton was assigned to the track with larger momentum and the mass of the pion to the other track;
- $0.48 < M(\pi^+\pi^-) < 0.52$ GeV.

⁴ $M(ab)$ is defined as the invariant mass for two vertex tracks with the assignment of masses of particles a and b .

The mass peaks for K_S^0 and $\Lambda + \bar{\Lambda}$ in the high- Q^2 sample are shown in Fig. 1. The decay of K_S^0 , Λ , and $\bar{\Lambda}$ was well understood as can be demonstrated by Fig. 2, which shows the proper decay times, reconstructed from the three dimensional decay length, compared to the expectations from MC simulation (see below).

4 Event simulation

Production of K_S^0 , Λ and $\bar{\Lambda}$ hadrons was modelled using the MC programs described below. In these models, strange quarks can be produced perturbatively by the boson-gluon fusion process ($\gamma g \rightarrow s\bar{s}$) or by gluon splitting in so-called parton showers. They may also originate from the proton parton densities or can be generated in non-perturbative string fragmentation. Strange hadrons are produced during hadronization, when quarks recombine into hadrons, and through the decays of other hadrons. Samples of events were generated to determine the response of the detector and obtain the correction factors required to convert the detector-level distributions to the hadron level. The generated events were passed through a full simulation of the detector, using GEANT 3.13 [35], and processed with the same reconstruction program as used for the data.

The high- Q^2 and the low- Q^2 DIS data were corrected to the hadron level using the ARIADNE 4 [8] MC program interfaced to HERACLES 4.6.1 [36–39] via DJANGO 1.1 [39], to include QED corrections. The CTEQ proton parton density functions were used [40,41]. ARIADNE is based on the Colour Dipole Model in which most QCD coherence effects are modelled as gluon emission from colour dipoles between partons. The program uses the Lund string model [42] to simulate the fragmentation of the partons. A significant parameter governing the production of strange hadrons is the strangeness-suppression factor, λ_s , that is probability to produce s -quark pairs relative to u - and d -quark pairs in the string fragmentation. This was set to 0.3, the default value, as found in e^+e^- annihilation [43]. Other parameters that control baryon production were set to their default values⁵ [44]. This ARIADNE sample was also used to compare to the final cross sections and ratios.

A value of λ_s smaller than 0.3 is often preferred [2, 4, 45] for K_S^0 production. Therefore, a further sample with $\lambda_s = 0.22$ [46] was also generated and used for comparison. The DIS data were additionally simulated using the LEPTO 6.5 MC program [9], which is based on first-order matrix elements plus parton showers (MEPS). The same Lund string

⁵ The key parameters for baryon production in JETSET are the diquark-antidiquark pair production suppression PARJ(1)=0.10, the suppression of s quark pair production compared to u or d pair production $\lambda_s \equiv$ PARJ(2)=0.30, the extra suppression of strange diquark production compared with the normal suppression of strange quarks PARJ(3)=0.4 and the suppression of spin 1 diquarks compared with spin 0 ones PARJ(4)=0.05.

model was used for the hadronisation, with $\lambda_s = 0.3$, and the same proton parton density functions as in the ARIADNE sample. This was used for further comparison to the data.

The photoproduction data were corrected to the hadron level using the PYTHIA 6 event generator [11], which consists of leading-order matrix-element calculations with initial- and final-state parton showering to simulate higher-order processes. The proton and photon PDFs were taken from GRV [47] and SaS2D [48] respectively. Multiple interactions [24,49,50], where more than one pair of partons (one parton from the photon and one parton from the proton) interact independently, were included. The default implementation was used, with the p_T^{min} [44] value of 2.7 GeV. The hadronisation is performed by the Lund string model, as in ARIADNE, with the same parameters controlling the production of strange hadrons. Direct and resolved events were generated separately. For correction of the data, the direct and resolved subsamples were combined such that they gave a best fit to the data x_γ^{OBS} distribution. The PYTHIA sample was also used to compare to the final cross sections and ratios, in which case the direct and resolved events were combined according to the predicted cross sections.

5 Cross-section determination

The cross sections in the high- Q^2 DIS sample were measured in the kinematic region $Q^2 > 25 \text{ GeV}^2$ and $0.02 < y < 0.95$. The cross sections in the low- Q^2 DIS sample were measured in the kinematic region $5 < Q^2 < 25 \text{ GeV}^2$ and $0.02 < y < 0.95$. The cross sections in the photoproduction sample were measured in the kinematic region $Q^2 < 1 \text{ GeV}^2$ and $0.2 < y < 0.85$, with the additional requirement of 2 jets, both satisfying $E_T^{\text{jet}} > 5 \text{ GeV}$ and $|\eta^{\text{jet}}| < 2.4$. In all three samples there was a further kinematic requirement that $0.6 < P_T^{\text{LAB}}(K_S^0, \Lambda, \bar{\Lambda}) < 2.5 \text{ GeV}$ and $|\eta^{\text{LAB}}(K_S^0, \Lambda, \bar{\Lambda})| < 1.2$. In all samples the measured cross sections were the luminosity-weighted average of the cross sections at the centre-of-mass energies $\sqrt{s} = 318 \text{ GeV}$ and $\sqrt{s} = 300 \text{ GeV}$. In the DIS samples differential cross sections were measured as functions of $P_T^{\text{LAB}}(K_S^0, \Lambda, \bar{\Lambda})$, $\eta^{\text{LAB}}(K_S^0, \Lambda, \bar{\Lambda})$, x_{Bj} , and Q^2 . In the photoproduction sample differential cross sections were measured as functions of $P_T^{\text{LAB}}(K_S^0, \Lambda, \bar{\Lambda})$, $\eta^{\text{LAB}}(K_S^0, \Lambda, \bar{\Lambda})$, and x_γ^{OBS} .

The K_S^0 , Λ and $\bar{\Lambda}$ differential cross sections in any variable Y were calculated using a standard bin-by-bin correction as follows:

$$\frac{d\sigma}{dY} = \frac{N}{A \cdot \mathcal{L} \cdot B \cdot \Delta Y},$$

where N is the number of K_S^0 , Λ or $\bar{\Lambda}$ in a bin of width ΔY , \mathcal{L} is the luminosity, A is the acceptance and B is the branching ratio. The acceptance was calculated from the MC samples described in Section 4, and took into account migration effects and efficiencies

for each bin. The acceptance for each particle was calculated for each bin of a 6×6 grid in p_T and η . An additional acceptance correction was made to obtain the differential cross sections as functions of variables other than p_T or η . In each bin a mass-sideband subtraction method was used to subtract the remaining combinatorial background in the K_S^0 , Λ and $\bar{\Lambda}$ samples, which was at the level of $\sim 3\%$ in the K_S^0 sample and $\sim 6\%$ in the Λ and $\bar{\Lambda}$ samples.

The differential cross sections, $\frac{d\sigma}{dY}$, for the considered particle as a function of η and P_T can be converted into the multiplicity distribution $\frac{1}{d\sigma_{\text{inc}}} \frac{d\sigma}{dY}$, where σ_{inc} is the inclusive event cross section using the following factors: $\sigma_{\text{inc}}^{-1} = 2.6 \times 10^{-5} \text{ pb}^{-1}$ for the high- Q^2 sample, $8.9 \times 10^{-6} \text{ pb}^{-1}$ for the low- Q^2 sample and $1.6 \times 10^{-5} \text{ pb}^{-1}$ for the photoproduction sample. On average, in the measured P_T and η region, for the high- Q^2 sample, there were about 0.017 Λ (or $\bar{\Lambda}$) and 0.09 K_S^0 per event. The corresponding multiplicities for the photoproduction sample were 0.077 for Λ (or $\bar{\Lambda}$) and 0.27 for K_S^0 .

5.1 Systematic uncertainties

The main sources which contributed to the systematic uncertainty were investigated by changing the analysis procedure, as outlined below, and observing the difference from the primary result. The total systematic uncertainty in the DIS samples for each bin was calculated by adding the individual contributions from the different variations in quadrature. The following sources of systematic uncertainties were considered: the energy measurement of the scattered electron; the measurement of Q^2 , δ , Z_{vtx} and y ; measurements of secondary-track p_T and η ; the removal of Λ and K_S^0 due to the collinearity cut; the impact position of the electron on the CAL; the estimation of the background. The systematic uncertainty on the cross sections was generally $\lesssim 5\%$. Additionally, a 2% uncertainty due to the luminosity measurement was included for the cross sections. The branching-ratio uncertainties were deemed negligible and not taken into account.

The most significant systematic error in the photoproduction sample was due to the uncertainty in the calorimeter energy scale ($\pm 3\%$), shown as a separate band in the figures. Typical uncertainties in the cross sections were $\lesssim 10\%$, except in the highest bin of x_γ^{OBS} where the uncertainty was up to 80%. A systematic uncertainty of 7% on the photoproduction cross sections due to trigger efficiencies was included. The limitations of the PYTHIA Monte Carlo simulation, particularly in describing the x_γ^{OBS} distribution in the data, introduced a possible additional systematic uncertainty in correcting the data from detector level to hadron level. The effect of this was investigated by reweighting the PYTHIA x_γ^{OBS} distribution to the data and using this reweighted sample to correct the data. The difference between the results obtained with the reweighted sample compared to the primary results was treated as a further systematic uncertainty; uncertainties in

the cross sections were $\lesssim 5\%$.

The uncertainty of the tracking simulation [51] was negligible compared to all other sources. Most of the uncertainties discussed above cancel in the ratios and asymmetries presented in this paper.

6 Results and discussion

6.1 Cross sections

Measured differential cross sections for the production of K_S^0 and $\Lambda + \bar{\Lambda}$ are shown in Figs. 3 - 6 for the DIS data and in Figs. 7 and 8 for the photoproduction sample. The DIS cross sections are compared to the absolute predictions of ARIADNE and LEPTO MC calculations. The photoproduction cross sections are compared to the prediction of the PYTHIA MC with multiple interactions normalised to the data cross section.

The ARIADNE program with strangeness-suppression factor of 0.3 describes the data reasonably well, although the K_S^0 cross section for the high- Q^2 sample is overestimated. The slope of the P_T^{LAB} dependence is incorrect and the cross section at low x_{Bj} is underestimated for both low- and high- Q^2 samples. A similar comment can be made for the $\Lambda + \bar{\Lambda}$ cross sections.

The description of the data by ARIADNE with the strangeness-suppression factor of 0.22 is less satisfactory but, as λ_s is not the only parameter influencing the cross section, a conclusion on what value of the λ_s can describe the data best can not be drawn. The LEPTO MC does not describe the data well.

In photoproduction, PYTHIA with multiple interactions describes the shape of the data dependence on P_T^{LAB} and η^{LAB} adequately, but the x_γ^{OBS} dependence is predicted to be too flat and at the smallest x_γ^{OBS} , in the resolved photon region, the description is poor.

6.2 Baryon-antibaryon asymmetry

The baryon-antibaryon asymmetry \mathcal{A} is defined as:

$$\mathcal{A} = \frac{N(\Lambda) - N(\bar{\Lambda})}{N(\Lambda) + N(\bar{\Lambda})},$$

where $N(\Lambda)$, $N(\bar{\Lambda})$ is the number of Λ and $\bar{\Lambda}$ baryons, respectively.

The baryon-antibaryon asymmetry \mathcal{A} has been measured and compared to MC predictions from ARIADNE and PYTHIA (with $\lambda_s = 0.3$ for both, and also with $\lambda_s = 0.22$ for ARIADNE). The following values were obtained:

- at high Q^2 : $\mathcal{A} = 0.3 \pm 1.3_{-0.8}^{+0.5}\%$, compared to the ARIADNE ($\lambda_s = 0.3$) prediction of $0.4 \pm 0.2\%$;
- at low Q^2 : $\mathcal{A} = 1.2 \pm 1.6_{-2.1}^{+0.7}\%$, compared to the ARIADNE ($\lambda_s = 0.3$) prediction of $1.0 \pm 0.2\%$;
- in photoproduction: $\mathcal{A} = -0.07 \pm 0.6_{-1.0}^{+1.0}\%$, compared to the PYTHIA prediction of $0.6 \pm 0.1\%$.

Figures 9 and 10 show the baryon-antibaryon asymmetry at high- Q^2 as a function of P_T^{LAB} , η^{LAB} , x_{Bj} , Q^2 and in photoproduction as a function of P_T^{LAB} , η^{LAB} and x_γ^{OBS} . In all cases, the average baryon-antibaryon asymmetry is consistent both with no asymmetry and consistent with the very small asymmetry predicted by Monte Carlo. This suggests that in the considered parts of the ep phase-space, to a good approximation, baryons and antibaryons are produced according to the same mechanism.

A positive asymmetry of 3.5% is predicted in DIS [13], due to the so called gluon-junction mechanism that makes it possible for the “baryon number to travel” several units of rapidity, in this case from the proton beam direction to the rapidity around 0 in the laboratory frame in which the measurements were made. Such a class of models can describe the significant positive baryon-antibaryon asymmetry which has been measured at the heavy-ion collider RHIC [52]. Although this prediction is not Q^2 dependent, it is not clear whether it could be extended down to $Q^2 = 0$ and applied to the selected photoproduction sample. Combining statistical and systematic errors from the three samples, the average asymmetry is in disagreement with the 3.5% value.

Although ARIADNE predicts that on average about 15% (40% at the highest x_{Bj} for the low- Q^2 sample) of events with a reconstructed Λ or $\bar{\Lambda}$ originate from the exchanged photon coupling to an s or \bar{s} quark from the proton, this measurement, being at low x_{Bj} , is not sensitive to the strange-quark asymmetry in the proton structure function as studied by NuTeV [53].

As our baryon-antibaryon asymmetry is consistent with no asymmetry, the Λ and $\bar{\Lambda}$ samples were combined together (except for the transverse polarization measurement) and results presented for the combined sample.

6.3 Baryon-to-meson ratio

The baryon-to-meson ratio \mathcal{R} is defined as:

$$\mathcal{R} = \frac{N(\Lambda) + N(\bar{\Lambda})}{N(K_S^0)},$$

where $N(\Lambda)$, $N(\bar{\Lambda})$, $N(K_S^0)$ refer to the number of indicated hadrons.

Figures 11 and 12 show the measured and predicted \mathcal{R} for the DIS samples as a function of P_T^{LAB} , η^{LAB} , x_{Bj} and Q^2 . The inaccuracies in describing the K_S^0 and $\Lambda + \bar{\Lambda}$ cross sections for high Q^2 , mentioned earlier, are clearly reflected in \mathcal{R} , but overall the ARIADNE MC with $\lambda_s = 0.3$ follows the shape of the data distributions and is usually in agreement to better than about 10%. The low- Q^2 sample is described by the same Monte Carlo programs with even better accuracy. In order to have a better understanding of how \mathcal{R} depends on x_{Bj} and Q^2 , \mathcal{R} is shown as a function of Q^2 for fixed bins in x_{Bj} and as a function of x_{Bj} for fixed bins in Q^2 in Figs. 13 and 14. A dependence on Q^2 and a discrepancy between the data and MC can now be seen for the bins of higher x_{Bj} . For the two bins of higher Q^2 , the MC underestimates the data at low x_{Bj} by up to 20%. The \mathcal{R} value varies between about 0.2 and 0.5, and is about 0.4 to 0.5 at low x_{Bj} and low Q^2 . These values can be compared to measurements at e^+e^- colliders, where for centre-of-mass energies from 10 to 200 GeV, \mathcal{R} varies between about 0.2 and 0.4 [34].

Figure 15 shows \mathcal{R} for the photoproduction sample. For the direct-enriched sample, where $x_\gamma^{\text{OBS}} > 0.75$, \mathcal{R} is about 0.4, the same value as in DIS at low x_{Bj} and low Q^2 . However, \mathcal{R} rises to a value of about 0.7 towards low x_γ^{OBS} (resolved-enriched sample), while it stays flat in the PYTHIA prediction.

In order to study this effect further, the photoproduction events were divided into two samples. In the first, the jet with the highest transverse energy was required to contribute at most 30% to the total hadronic transverse energy. In this sample the events have largely isotropic transverse energy flow and therefore the sample is called “fireball-enriched”. The other sample, containing all the other events, was called “fireball-depleted”. Figure 16(a) shows the distribution of events as a function of the total transverse energy, which is on average 30 GeV, and of the transverse energy of the jet with the highest E_T^{jet} . The line represents the cut used to separate fireball-enriched and fireball-depleted samples. Figure 16(b) illustrates the fireball selection in relation to the fraction of the total transverse energy carried by two jets of the highest transverse energy. It can be seen that fireball-depleted events are dominated by dijet events carrying most of the total transverse energy and that the fireball-enriched and fireball-depleted samples have about the same number of events.

The baryon-to-meson ratios for the fireball-enriched and fireball-depleted samples are presented in Fig. 17 for the data and PYTHIA MC. The measured \mathcal{R} is larger for the fireball-enriched sample, most significantly at high P_T^{LAB} , than it is for the fireball-depleted sample. This feature is not reproduced by PYTHIA, which predicts almost the same \mathcal{R} for both samples. The PYTHIA prediction reasonably describes the measured values of \mathcal{R} for the fireball-depleted sample. This is not surprising as PYTHIA generates jets in events according to the multiple interaction mechanism [49], which makes several independent jets, like those in DIS or e^+e^- where baryons and mesons are created locally. Provided

there is enough energy available, \mathcal{R} will be the same, regardless of the number of jets (ignoring some differences in quark and gluon fragmentation).

Large values of \mathcal{R} , larger than 1, have been measured at hadron and heavy-ion colliders: $p\bar{p}$ [6], pp [7, 54] and RHIC [55–58].

6.4 Ratio of strange-to-light hadrons

The ratio of strange-to-light hadrons was measured in terms of \mathcal{T} :

$$\mathcal{T} = \frac{N(K_S^0)}{N_{\text{ch}}},$$

where $N(K_S^0)$ is the number of K_S^0 and N_{ch} is the number of charged pions, charged kaons, protons and antiprotons, (excluding products of K_S^0 , Λ , and $\bar{\Lambda}$ decays) in the same region of P_T^{LAB} and η^{LAB} as the K_S^0 .

In Figs. 18 and 19, \mathcal{T} is shown as a function of P_T^{LAB} and η^{LAB} for the high- Q^2 sample (for the low- Q^2 sample, not shown, the values are similar) and for the photoproduction sample. The MC predictions from ARIADNE and PYTHIA are also shown. They follow the data reasonably well, preferring the strangeness-suppression factor to be smaller than 0.3. The measured \mathcal{T} lies between 0.05 and 0.1, varying with P_T^{LAB} for both the DIS and photoproduction. Similar values have been measured at e^+e^- [34] for the ratio of the number of K_S^0 to the number of charged pions and are on average about 0.07 at centre-of-mass energies from 10 to 35 GeV, about 0.06 at the Z^0 and about 0.05 at 200 GeV. It can be concluded that \mathcal{T} is about the same in e^+e^- and ep .

In order to see whether \mathcal{T} depends on the transverse energy flow, the fireball selection, as discussed above, was applied to the photoproduction events. Figures 19(c) and (d) show the measured and predicted \mathcal{T} for the fireball selection. The quantity \mathcal{T} hardly depends on the fireball selection, as predicted by PYTHIA.

Fireball events are candidates for events where QCD instantons [15–17] could play a role [59–61], since they are characterised by isotropic transverse energy flow. Another expectation is a likely enhancement of heavier-quark production relative to light quarks, due to the required flavour democracy. Searches for QCD instantons in DIS have been reported by H1 [62] and ZEUS [63]. No effect was identified due to QCD instantons, as the expected effects were small compared to the background at the relatively large Q^2 required. Bigger effects are expected at lower Q^2 .

If QCD instantons contribute to the fireball event sample, then \mathcal{T} would be expected to be different, possibly larger, for the fireball events than the typical value of about 0.07 or 0.08. As this is not the case, this measurement of \mathcal{T} in photoproduction does not support

the idea that QCD instantons contribute significantly to the production of the fireball events. It should be noted that there is only a qualitative prediction on the contribution from QCD instantons based on democracy of flavours, including heavy flavours, subject to available energy. The only existing calculation [61] applies to DIS and only considers three massless flavours. Since there is no charm-quark contribution, this calculation is probably only valid at low particle multiplicities, where the number of K_S^0 is predicted to be about twice as big as that predicted by ARIADNE.

6.5 Polarization

In analogy with QED, the spin-orbit interaction leads to polarization in scattering due to the strong interaction [18–20]. Unpolarized s quarks get partially transversely polarized due to elastic scattering in the coloured field along the direction of $k_i \times k_f$, where k_i and k_f stand for the initial and final momenta of the s quarks. The degree of the polarization depends on the scattering angle and the strength of the coloured field. In the constituent quark model, the Λ inherits its spin from the s quark, and k_f is along the Λ momentum. As k_i is unknown in our case, the electron beam direction was used instead (the effect of using the jet direction was also investigated).

The transverse polarization \mathcal{P}^Λ ($\mathcal{P}^{\bar{\Lambda}}$) is defined by the form of the proton (antiproton) angular distribution:

$$\frac{1}{N} \frac{dN}{d \cos \theta} = \frac{1}{2} [1 + \alpha \mathcal{P}^\Lambda \cos \theta],$$

$$\frac{1}{N} \frac{dN}{d \cos \theta} = \frac{1}{2} [1 - \alpha \mathcal{P}^{\bar{\Lambda}} \cos \theta],$$

where α is the decay asymmetry parameter, measured to be $\alpha = 0.642 \pm 0.013$ [34], and θ is the angle between the proton (antiproton) momentum boosted to the rest frame of the $\Lambda(\bar{\Lambda})$ and the polarization axis, $k_e^{\text{beam}} \times k_\Lambda$. An example of the angular distribution of the proton's (antiproton's) momenta with respect to the polarization axis, boosted to the $\Lambda(\bar{\Lambda})$ rest frame, is shown in Fig. 20.

Fitted values of the transverse polarization \mathcal{P}^Λ and $\mathcal{P}^{\bar{\Lambda}}$ are presented in Table 1 for high- and low- Q^2 DIS and for photoproduction. All values are compatible with no polarization. Also presented are the polarization values obtained by investigating the angular distribution of the higher-momentum π from K_S^0 decays, as a further test of any systematic detector effect.

7 Conclusions

Measurements of K_S^0 , Λ and $\bar{\Lambda}$ production have been made at HERA, using 121 pb^{-1} of data collected with the ZEUS detector. The following conclusions have been obtained:

1. in high- and low- Q^2 DIS, ARIADNE reproduces gross features of the cross sections but shows discrepancies in detail. Overall, the strangeness suppression factor $\lambda_s = 0.3$ is preferred to $\lambda_s = 0.22$. PYTHIA, normalised to the data, describes the dependence of the photoproduction cross sections on P_T^{LAB} and η^{LAB} satisfactorily but fails to reproduce the x_γ^{OBS} dependence;
2. the numbers of Λ and $\bar{\Lambda}$ produced are consistent with being equal;
3. except for the resolved photon interactions, the measured ratio of baryons to mesons \mathcal{R} , defined as:

$$\mathcal{R} = \frac{N(\Lambda) + N(\bar{\Lambda})}{N(K_S^0)},$$

is in the range between 0.2 and 0.5, similar to measurements at e^+e^- colliders. ARIADNE and PYTHIA follow the shapes of the data on the selected observables but in many cases fail quantitatively at the 10 to 20% level;

4. in the resolved photon region, the ratio of baryons to mesons is large, significantly larger than measured in e^+e^- interactions and significantly larger than the PYTHIA prediction;
5. the ratio of strange-to-light hadrons measured in terms of \mathcal{T} :

$$\mathcal{T} = \frac{N(K_S^0)}{N_{\text{ch}}},$$

is compatible with measurements at other colliders and is described by ARIADNE and PYTHIA for all investigated samples of events. For the DIS sample, the strangeness suppression factor $\lambda_s = 0.22$ is preferred to the default value of $\lambda_s = 0.3$. For the photoproduction sample, PYTHIA with $\lambda_s = 0.3$ overestimates the data, but describes the shape of the distributions. There is no indication of any unusual yield of strange-hadrons in the fireball-enriched sample, as would be qualitatively expected had there been a significant contribution from QCD instantons;

6. No evidence has been found for non-zero transverse polarization in inclusive Λ or $\bar{\Lambda}$ production.

8 Acknowledgments

We thank the DESY directorate for its strong support and encouragement. The remarkable achievements of the HERA machine group were essential for the successful completion of this work and are greatly appreciated. The design, construction and installation of the ZEUS detector have been made possible by the efforts of many people who are not listed as authors.

References

- [1] TASSO Coll., M. Althoff et al., *Z. Phys. C* **27**, 27 (1985);
TASSO Coll., W. Braunschweig et al., *Z. Phys. C* **47**, 167 (1990);
TPC Coll., H. Aihara et al., *Phys. Rev. Lett.* **54**, 274 (1985);
MARK-II Coll., C. De La Vaissiere et al., *Phys. Rev. Lett.* **54**, 2071 (1985);
MARK-II Coll., H. Schellman et al., *Phys. Rev. D* **31**, 3013 (1985);
HRS Coll., M. Derrick et al., *Phys. Rev. D* **35**, 2639 (1987);
TASSO Coll., R. Brandelik et al., *Phys. Lett. B* **105**, 75 (1981);
TASSO Coll., W. Braunschweig et al., *Z. Phys. C* **45**, 209 (1989);
CELLO Coll., H. Behrend et al., *Z. Phys. C* **46**, 397 (1990);
ALEPH Coll., D. Buskulic et al., *Z. Phys. C* **64**, 361 (1994);
DELPHI Coll., P. Abreu et al., *Phys. Lett. B* **318**, 249 (1993).
- [2] DELPHI Coll., P. Abreu et al., *Z. Phys. C* **65**, 587 (1995).
- [3] L3 Coll., M. Acciarri et al., *Phys. Lett. B* **328**, 223 (1994);
OPAL Coll., P. Acton et al., *Phys. Lett. B* **291**, 503 (1992);
OPAL Coll., R. Akers et al., *Z. Phys. C* **67**, 389 (1995).
- [4] ZEUS Coll., M. Derrick et al., *Z. Phys. C* **68**, 29 (1995);
ZEUS Coll., J. Breitweg et al., *Eur. Phys. J. C* **2**, 77 (1998);
H1 Coll., S. Aid et al., *Nucl. Phys. B* **480**, 3 (1996);
H1 Coll., C. Adloff et al., *Z. Phys. C* **76**, 213 (1997).
- [5] UA5 Coll., R. Ansorge et al., *Z. Phys. C* **41**, 179 (1988);
UA5 Coll., R. Ansorge et al., *Nucl. Phys. B* **328**, 36 (1989);
CDF Coll., D. Acosta et al., *Phys. Rev. D* **72**, 052001 (2005).
- [6] UA1 Coll., G. Bocquet et al., *Phys. Lett. B* **366**, 441 (1996).
- [7] STAR Coll., B.I. Abelev et al., Preprint nucl-ex/0607033, 2006.
- [8] L. Lönnblad, *Comp. Phys. Comm.* **71**, 15 (1992).
- [9] G. Ingelman, A. Edin and J. Rathsman, *Comp. Phys. Comm.* **101**, 108 (1997).
- [10] H. Jung, *Comp. Phys. Comm.* **86**, 147 (1995).
- [11] T. Sjöstrand et al., *Comp. Phys. Comm.* **135**, 238 (2001).
- [12] G. Corcella et al., Preprint hep-ph/0210213, 2002.
- [13] B. Kopeliovich and B. Povh, *Z. Phys. C* **75**, 693 (1997).
- [14] R. Fries et al., *Phys. Rev. Lett.* **90**, 202303 (2003);
S. Bass, B. Müller and D. Srivastava, *Phys. Rev. Lett.* **91**, 052302 (2003).
- [15] A. Belavin et al., *Phys. Lett. B* **59**, 85 (1975).

- [16] G. 't Hooft, Phys. Rev. Lett. **37**, 8 (1976);
G. 't Hooft, Phys. Rev. **D 14**, 3432 (1976);
G. 't Hooft, Phys. Rev. **D 18**, 2199 (1978);
G. 't Hooft, Phys. Rep. **142**, 357 (1986).
- [17] H. Aoyama and H. Goldberg, Phys. Lett. **B 188**, 506 (1987);
A. Ringwald, Nucl. Phys. **B 330**, 1 (1990);
O. Espinosa, Nucl. Phys. **B 343**, 310 (1990);
A. Ringwald et al., Nucl. Phys. **B 365**, 3 (1991);
M. Gibbs et al., Z. Phys. **C 66**, 285 (1995);
A. Ringwald, Phys. Lett. **B 555**, 227 (2002).
- [18] J. Szwed, Phys. Lett. **B 105**, 403 (1981).
- [19] A. Panagiotou, Int. J. Mod. Phys. **A 5**, 1197 (1989).
- [20] J. Gago, R. Vilela Mendes and P. Vaz, Phys. Lett. **B 183**, 357 (1987).
- [21] ZEUS Coll., U. Holm (ed.), *The ZEUS Detector*. Status Report (unpublished), DESY (1993), available on <http://www-zeus.desy.de/bluebook/bluebook.html>.
- [22] N. Harnew et al., Nucl. Inst. Meth. **A 279**, 290 (1989);
B. Foster et al., Nucl. Phys. Proc. Suppl. **B 32**, 181 (1993);
B. Foster et al., Nucl. Inst. Meth. **A 338**, 254 (1994).
- [23] M. Derrick et al., Nucl. Inst. Meth. **A 309**, 77 (1991);
A. Andresen et al., Nucl. Inst. Meth. **A 309**, 101 (1991);
A. Caldwell et al., Nucl. Inst. Meth. **A 321**, 356 (1992);
A. Bernstein et al., Nucl. Inst. Meth. **A 336**, 23 (1993).
- [24] ZEUS Coll., J. Breitweg et al., Eur. Phys. J. **C 1**, 109 (1998).
- [25] J. Andruszków et al., Preprint DESY-92-066, DESY, 1992;
ZEUS Coll., M. Derrick et al., Z. Phys. **C 63**, 391 (1994);
J. Andruszków et al., Acta Phys. Pol. **B 32**, 2025 (2001).
- [26] H. Abramowicz, A. Caldwell and R. Sinkus, Nucl. Inst. Meth. **A 365**, 508 (1995);
R. Sinkus and T. Voss, Nucl. Inst. Meth. **A 391**, 360 (1997).
- [27] J.D. Bjorken and E.A. Paschos, Phys. Rev. **185**, 1775 (1969).
- [28] S. Bentvelsen, J. Engelen and P. Kooijman, *Proc. Workshop on Physics at HERA*, W. Buchmüller and G. Ingelman (eds.), Vol. 1, p. 23. Hamburg, Germany, DESY (1992);
K.C. Höger, *Proc. Workshop on Physics at HERA*, W. Buchmüller and G. Ingelman (eds.), Vol. 1, p. 43. Hamburg, Germany, DESY (1992).

- [29] F. Jacquet and A. Blondel, *Proceedings of the Study for an ep Facility for Europe*, U. Amaldi (ed.), p. 391. Hamburg, Germany (1979). Also in preprint DESY 79/48.
- [30] S. Catani et al., Phys. Lett. **B 285**, 291 (1992);
S. Catani et al., Nucl. Phys. **B 406**, 187 (1993).
- [31] S.D. Ellis and D.E. Soper, Phys. Rev. **D 48**, 3160 (1993).
- [32] ZEUS Coll., J. Breitweg et al., Eur. Phys. J. **C 11**, 35 (1999).
- [33] P. Billoir and S. Qian, Nucl. Inst. Meth. **A 311** (1992).
- [34] Particle Data Group, S. Eidelman et al., Phys. Lett. **B 592**, 1 (2004).
- [35] R. Brun et al., GEANT3, Technical Report CERN-DD/EE/84-1, CERN, 1987.
- [36] A. Kwiatkowski, H. Spiesberger and H.-J. Möhring, Comp. Phys. Comm. **69**, 155 (1992).
- [37] K. Charchula, G.A. Schuler and H. Spiesberger, Comp. Phys. Comm. **81**, 381 (1994).
- [38] H. Spiesberger, *An Event Generator for ep Interactions at HERA Including Radiative Processes (Version 4.6)*, 1996, available on <http://www.desy.de/~hspiesb/heracles.html>.
- [39] H. Spiesberger, *HERACLES and DJANGO: Event Generation for ep Interactions at HERA Including Radiative Processes*, 1998, available on <http://www.desy.de/~hspiesb/djangoh.html>.
- [40] H.L. Lai et al., Phys. Rev. **D 55**, 1280 (1997).
- [41] CTEQ Coll., H.L. Lai et al., Eur. Phys. J. **C 12**, 375 (2000).
- [42] B. Andersson et al., Phys. Rep. **97**, 31 (1983).
- [43] OPAL Coll., P.D. Acton et al., Z. Phys. **C 56**, 521 (1992);
OPAL Coll., R. Akers et al., Z. Phys. **C 68**, 1 (1995);
ALEPH Coll., D. Buskulic et al., Z. Phys. **C 69**, 379 (1996);
DELPHI Coll., P. Abreu et al., Z. Phys. **C 73**, 61 (1996).
- [44] T. Sjöstrand, L. Lönnblad and S. Mrenna, Preprint hep-ph/0108264, 2001.
- [45] E665 Coll., M. Adams et al., Z. Phys. **C 61**, 539 (1994);
SLD Coll., K. Abe et al., Phys. Rev. **D 59**, 052001 (1999).
- [46] ZEUS Coll., S. Chekanov et al., Phys. Lett. **B 553**, 141 (2002).
- [47] M. Glück, E. Reya and A. Vogt, Z. Phys. **C 67**, 433 (1995).
- [48] G.A. Schuler and T. Sjöstrand, Z. Phys. **C 68**, 607 (1995).
- [49] T. Sjöstrand and M. van Zijl, Phys. Rev. **D 36**, 2019 (1987);
G. Schuler and T. Sjöstrand, Phys. Lett. **B 300**, 169 (1993);

- G. Schuler and T. Sjöstrand, Nucl. Phys. **B 407**, 539 (1993);
J. Butterworth and J. Forshaw, J. Phys. **G 19**, 1657 (1993).
- [50] H1 Coll., S. Aid et al., Z. Phys. **C 70**, 17 (1996).
- [51] ZEUS Coll., S. Chekanov et al., Eur. Phys. J. **C 44**, 351 (2005).
- [52] PHENIX Coll., K. Adcox et al., Phys. Rev. Lett. **89**, 092302 (2002).
- [53] NuTeV Coll., M. Goncharov et al., submitted to Phys. Rev. **D** (2006).
- [54] STAR Coll., J. Adams et al., Phys. Lett. **B 637**, 161 (2006).
- [55] PHENIX Coll., S. Adler et al., Phys. Rev. **C 69**, 034909 (2004).
- [56] STAR Coll., C. Adler et al., Phys. Rev. Lett. **89**, 092301 (2002).
- [57] STAR Coll., J. Adams et al., Phys. Rev. Lett. **92**, 112301 (2004).
- [58] STAR Coll., J. Adams et al., Phys. Lett. **B 595**, 143 (2004).
- [59] A. Ringwald and F. Schrempp, Preprint hep-ph/9411217, 1994.
- [60] C. Nath, R. Walczak and Y. Yamazaki, J. Phys. **G 25**, 1440 (1999).
- [61] T. Carli et al., Preprint hep-ph/9906441, 1999.
- [62] H1 Coll., C. Adloff et al., Eur. Phys. J. **C 25**, 495 (2002).
- [63] ZEUS Coll., S. Chekanov et al., Eur. Phys. J. **C 34**, 255 (2004).

	Polarization (%)		
	High- Q^2 DIS	Low- Q^2 DIS	Photoproduction
Λ	$-1.3 \pm 4.3(stat.)_{-0.8}^{+4.0}(syst.)$	$-4.0 \pm 5.3(stat.)_{-4.0}^{+4.7}(syst.)$	$-2.4 \pm 2.2(stat.)$
$\bar{\Lambda}$	$-2.2 \pm 4.2(stat.)_{-1.3}^{+2.4}(syst.)$	$-8.5 \pm 5.5(stat.)_{-2.1}^{+4.7}(syst.)$	$-5.8 \pm 2.2(stat.)$
K_S^0	$-1.5 \pm 1.1(stat.)$	$-0.05 \pm 1.5(stat.)$	$-0.5 \pm 0.2(stat.)$

Table 1: The transverse polarization values for Λ and $\bar{\Lambda}$, expressed here in %, in the high- Q^2 DIS ($Q^2 > 25 \text{ GeV}^2$ and $0.02 < y < 0.95$), low- Q^2 DIS ($5 < Q^2 < 25 \text{ GeV}^2$ and $0.02 < y < 0.95$), and photoproduction ($Q^2 < 1 \text{ GeV}^2$, $0.2 < y < 0.85$ and with two jets $E_T^{\text{jet}} > 5 \text{ GeV}$ and $|\eta^{\text{jet}}| < 2.4$) samples. Only Λ and $\bar{\Lambda}$ in the range $0.6 < P_T^{\text{LAB}} < 2.5 \text{ GeV}$ and $|\eta^{\text{LAB}}| < 1.2$ are considered. The statistical error is quoted for all samples, together with the systematic uncertainty associated with the measurement for the high- Q^2 and low- Q^2 samples. A similar systematic uncertainty is expected for the photoproduction sample. Also shown, as a test of any systematic effect, are the polarization values obtained by investigating the angular distribution of the higher-momentum π from K_S^0 decays.

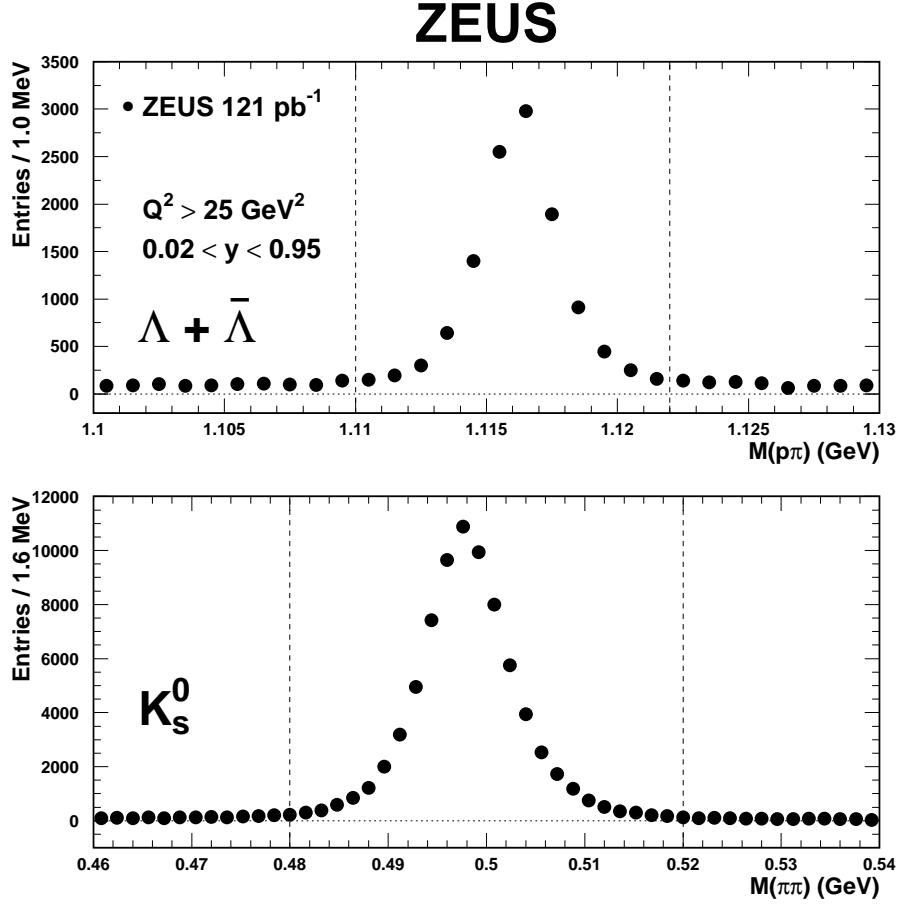


Figure 1: Mass distributions of the secondary vertex candidates in the $\Lambda + \bar{\Lambda}$ and K_S^0 samples assuming $p\pi$ and $\pi\pi$ decays respectively. Only candidates in the range $0.6 < P_T^{\text{LAB}} < 2.5 \text{ GeV}$ and $|\eta^{\text{LAB}}| < 1.2$ for events with $Q^2 > 25 \text{ GeV}^2$ and $0.02 < y < 0.95$ are displayed. Statistical errors are smaller than the point size. The number of total $\Lambda + \bar{\Lambda}$ and K_S^0 candidates located within the vertical lines are estimated to be 10731 and 73140, respectively, after the background subtraction.

ZEUS

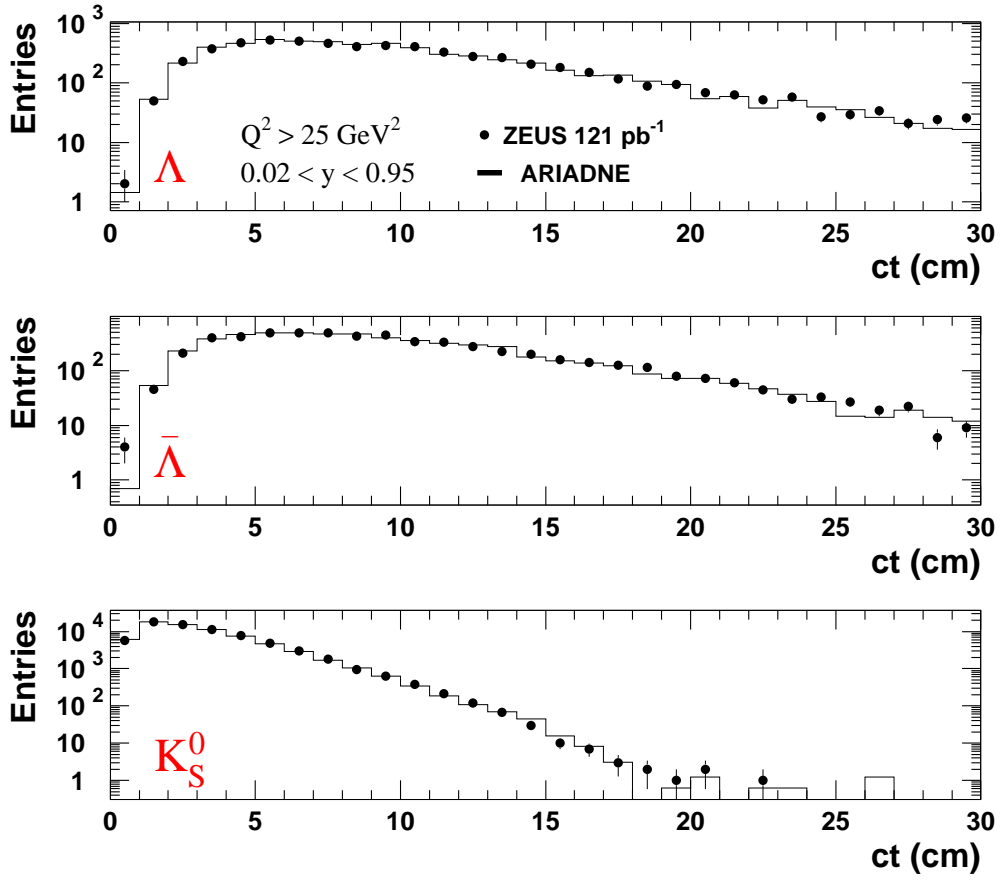


Figure 2: *Detector-level distributions of ct , where t is the reconstructed proper lifetime, for Λ , $\bar{\Lambda}$ and K_S^0 samples for data and ARIADNE. The ARIADNE histogram is normalised to the same number of events as the data. Statistical errors are shown unless smaller than the point size.*

ZEUS

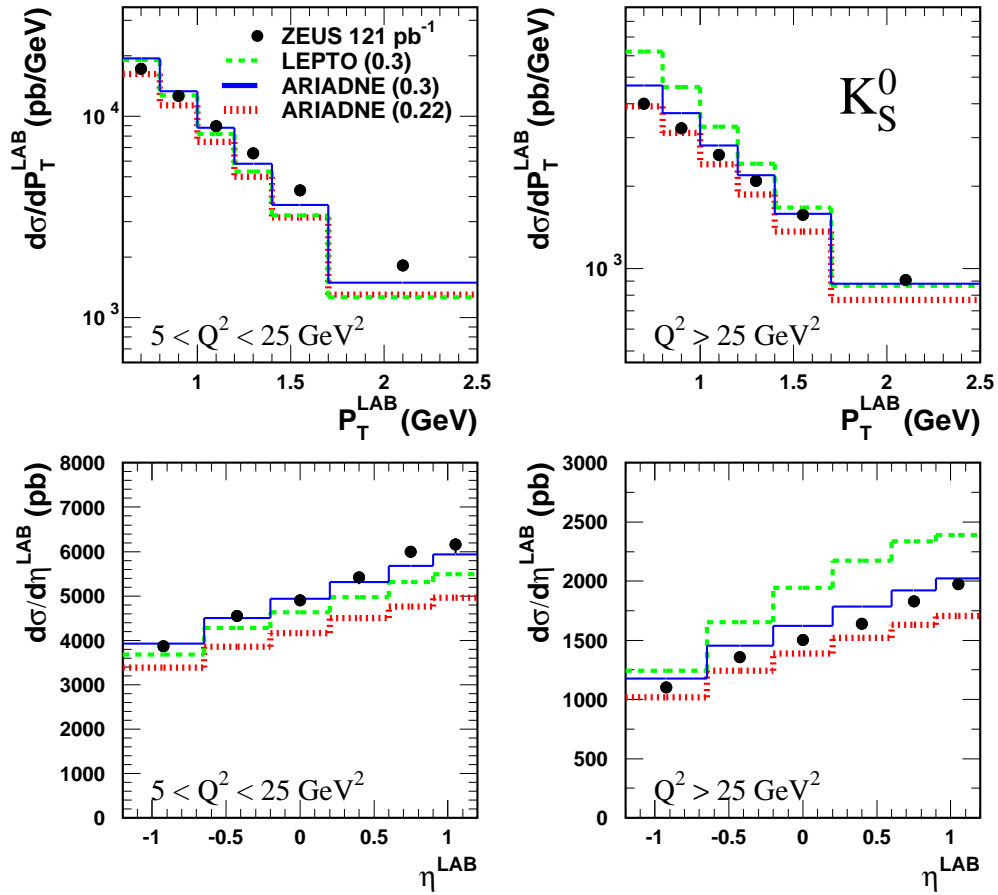


Figure 3: *Differential K_S^0 cross-sections as a function of P_T^{LAB} and η^{LAB} in the range $0.6 < P_T^{\text{LAB}} < 2.5 \text{ GeV}$ and $|\eta^{\text{LAB}}| < 1.2$ for events with $5 < Q^2 < 25 \text{ GeV}^2$, $0.02 < y < 0.95$ and $Q^2 > 25 \text{ GeV}^2$, $0.02 < y < 0.95$. Statistical errors (inner error bars) and the systematic uncertainties added in quadrature are shown, unless smaller than the point size. The histograms show predictions from ARIADNE and LEPTO using the stated strangeness suppression.*

ZEUS

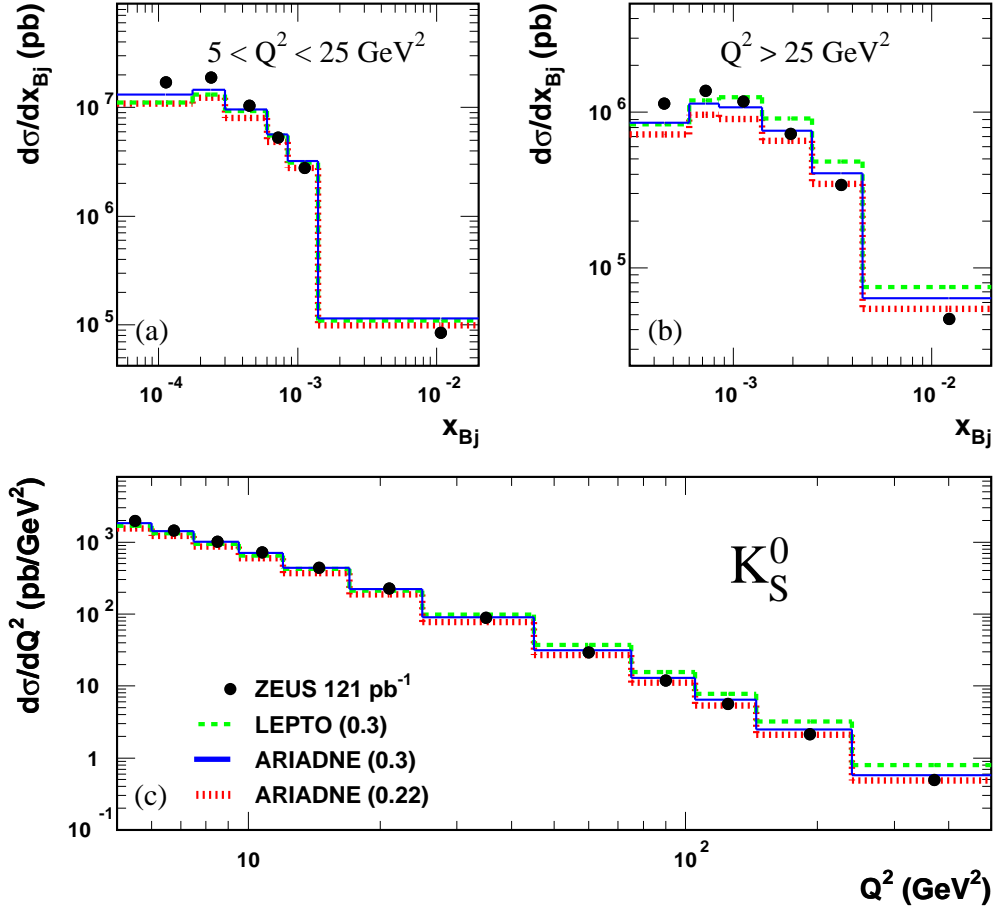


Figure 4: *Differential K_S^0 cross sections as a function of x_{Bj} and Q^2 in the range $0.6 < P_T^{\text{LAB}} < 2.5 \text{ GeV}$ and $|\eta^{\text{LAB}}| < 1.2$ for events a) with $5 < Q^2 < 25 \text{ GeV}^2$, $0.02 < y < 0.95$ b) $Q^2 > 25 \text{ GeV}^2$, $0.02 < y < 0.95$ and c) $Q^2 > 5 \text{ GeV}^2$, $0.02 < y < 0.95$. Statistical errors and the systematic uncertainties added in quadrature are smaller than the point size. The histograms show predictions from ARIADNE and LEPTO using the stated strangeness suppression.*

ZEUS

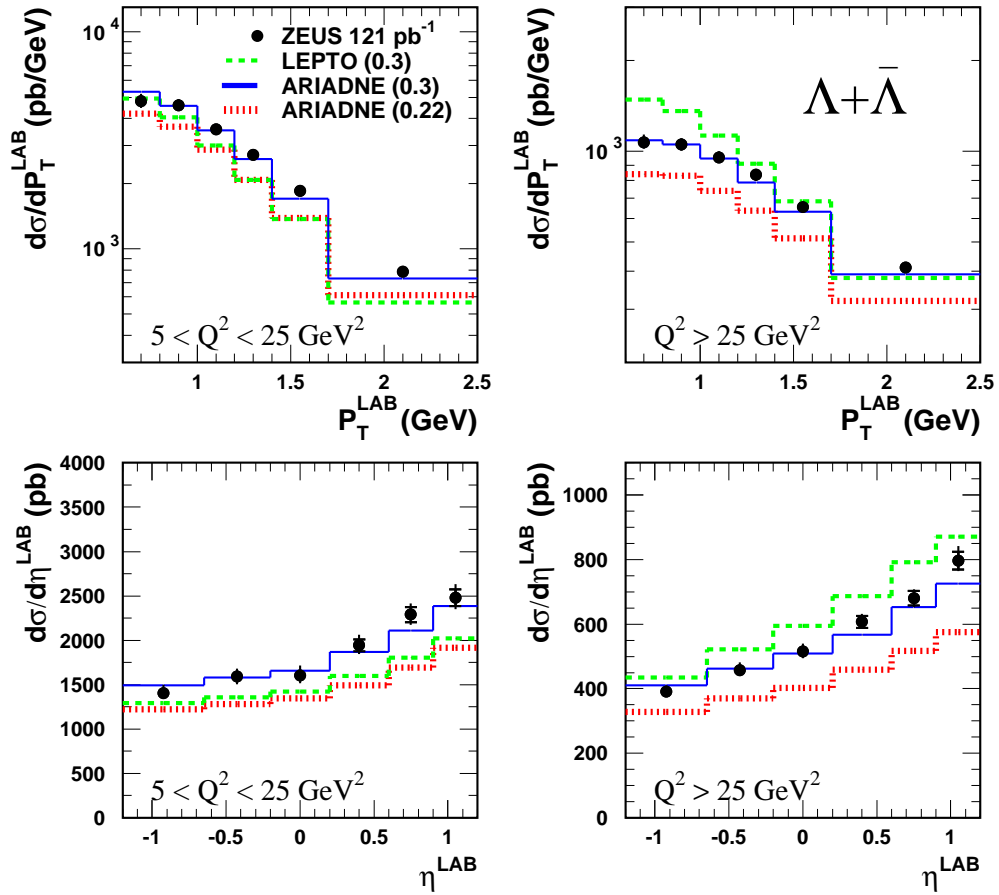


Figure 5: Differential $\Lambda + \bar{\Lambda}$ cross sections as a function of P_T^{LAB} and η^{LAB} in the range $0.6 < P_T^{\text{LAB}} < 2.5 \text{ GeV}$ and $|\eta^{\text{LAB}}| < 1.2$ for events with $5 < Q^2 < 25 \text{ GeV}^2$, $0.02 < y < 0.95$ and $Q^2 > 25 \text{ GeV}^2$, $0.02 < y < 0.95$. Statistical errors (inner error bars) and the systematic uncertainties added in quadrature are shown, unless smaller than the point size. The histograms show predictions from ARIADNE and LEPTO using the stated strangeness suppression.

ZEUS

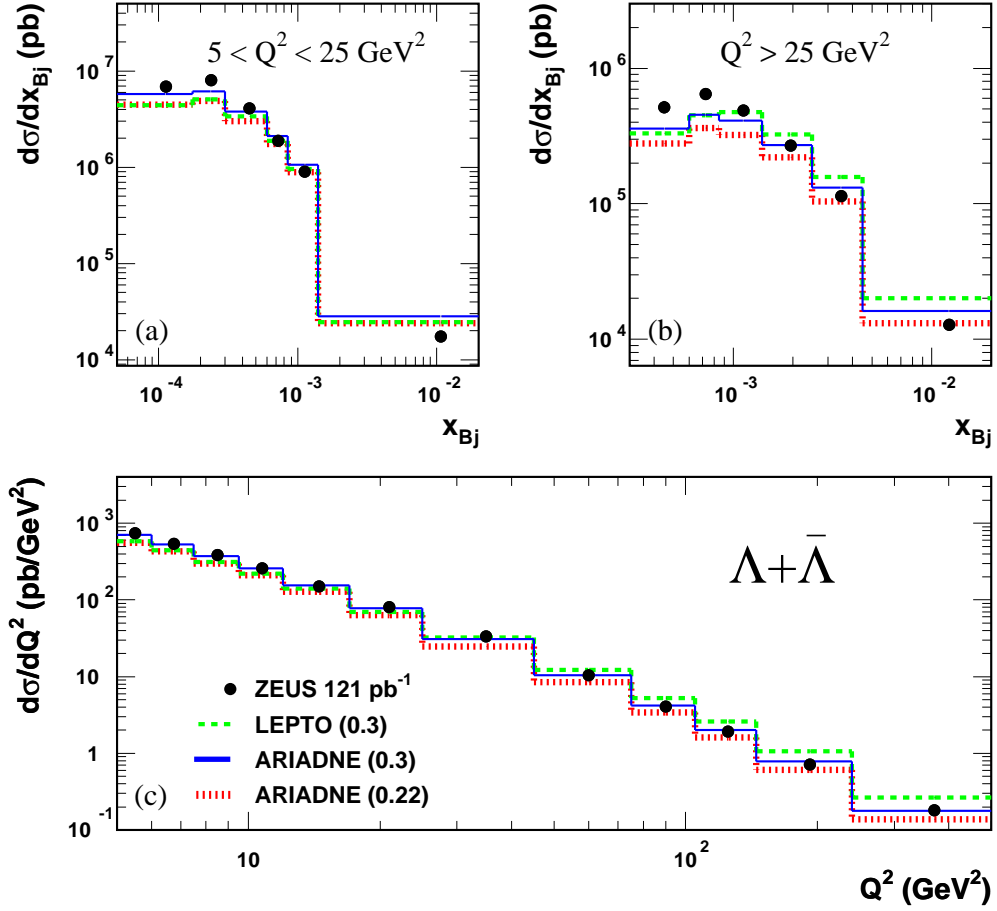


Figure 6: *Differential $\Lambda + \bar{\Lambda}$ cross sections as a function of x_{Bj} and Q^2 in the range $0.6 < P_T^{\text{LAB}} < 2.5 \text{ GeV}$ and $|\eta^{\text{LAB}}| < 1.2$ for events a) with $5 < Q^2 < 25 \text{ GeV}^2$, $0.02 < y < 0.95$ b) $Q^2 > 25 \text{ GeV}^2$, $0.02 < y < 0.95$ and c) $Q^2 > 5 \text{ GeV}^2$, $0.02 < y < 0.95$. Statistical errors and the systematic uncertainties added in quadrature are smaller than the point size. The histograms show predictions from ARIADNE and LEPTO using the stated strangeness suppression.*

ZEUS

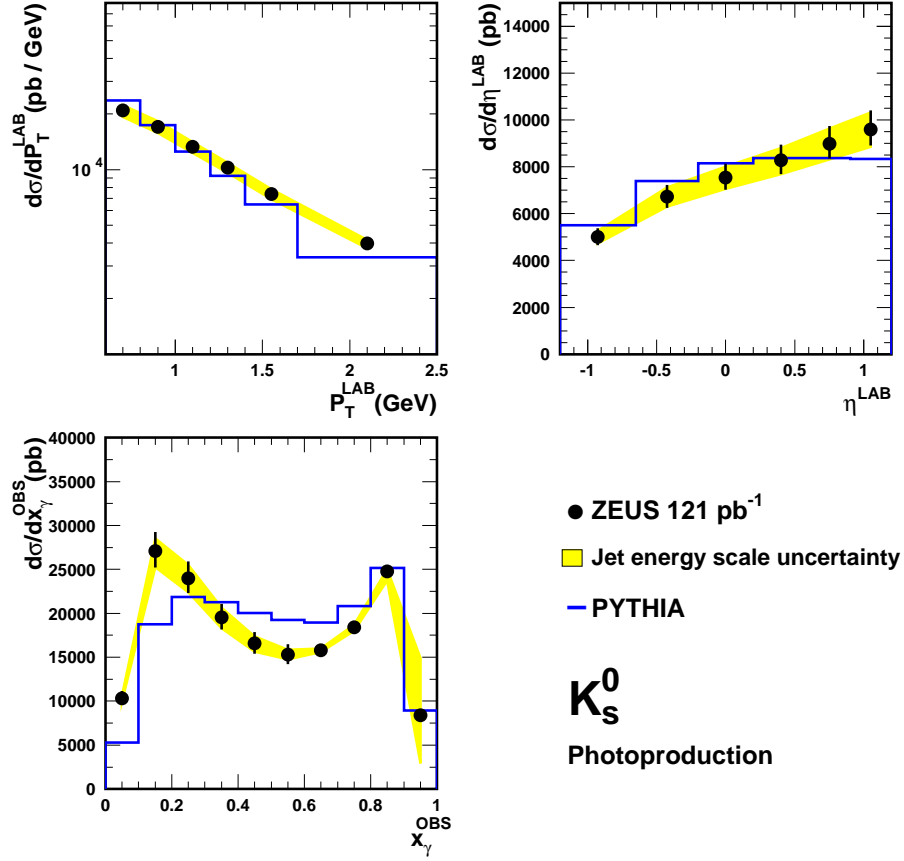


Figure 7: Differential K_S^0 cross sections as a function of P_T^{LAB} , η^{LAB} and x_γ^{OBS} , in the range $0.6 < P_T^{\text{LAB}} < 2.5$ GeV and $|\eta^{\text{LAB}}| < 1.2$ for events with $Q^2 < 1$ GeV^2 , $0.2 < y < 0.85$ and at least two jets both satisfying $E_T^{\text{jet}} > 5$ GeV and $|\eta^{\text{jet}}| < 2.4$. Statistical errors are shown, unless smaller than the point size, together with the systematic uncertainty arising from the trigger efficiency added in quadrature. The uncertainty arising from the jet energy scale is also shown (shaded band). The solid histogram shows the prediction from PYTHIA (with multiple interactions), normalised to the data.

ZEUS

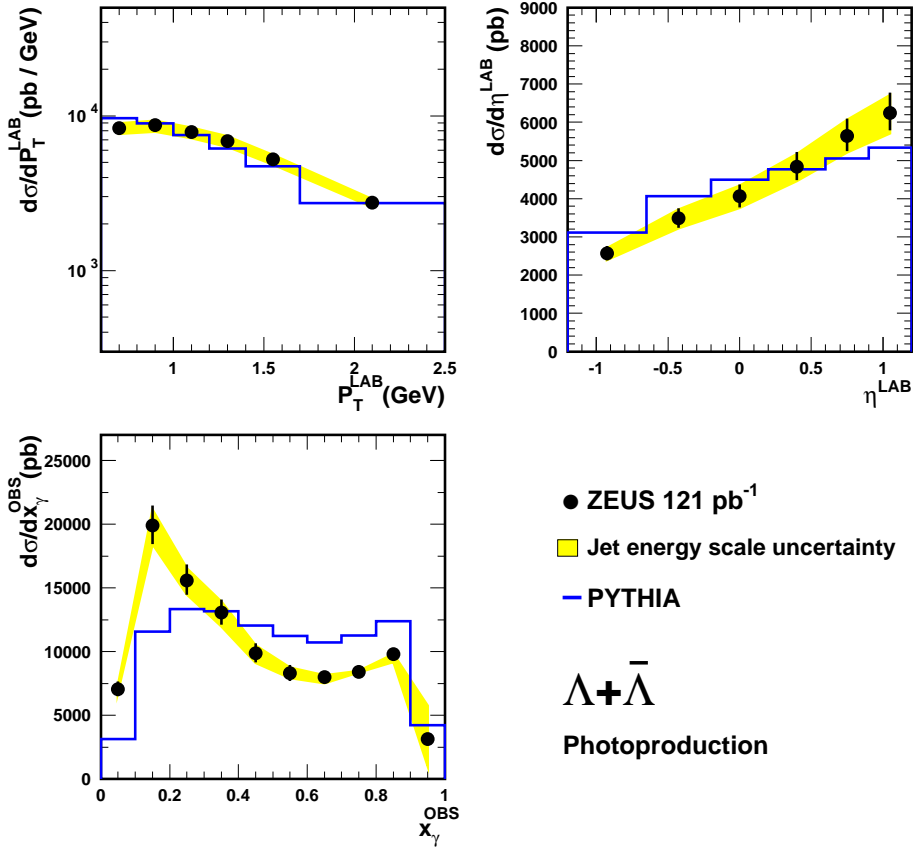


Figure 8: Differential $\Lambda + \bar{\Lambda}$ cross sections as a function of P_T^{LAB} , η^{LAB} and x_γ^{OBS} , in the range $0.6 < P_T^{\text{LAB}} < 2.5 \text{ GeV}$ and $|\eta^{\text{LAB}}| < 1.2$ for events with $Q^2 < 1 \text{ GeV}^2$, $0.2 < y < 0.85$ and at least two jets both satisfying $E_T^{\text{jet}} > 5 \text{ GeV}$ and $|\eta^{\text{jet}}| < 2.4$. Statistical errors are shown, unless smaller than the point size, together with the systematic uncertainty arising from the trigger efficiency added in quadrature. The uncertainty arising from the jet energy scale is also shown (shaded band). The solid histogram shows the prediction from PYTHIA (with multiple interactions), normalised to the data.

ZEUS

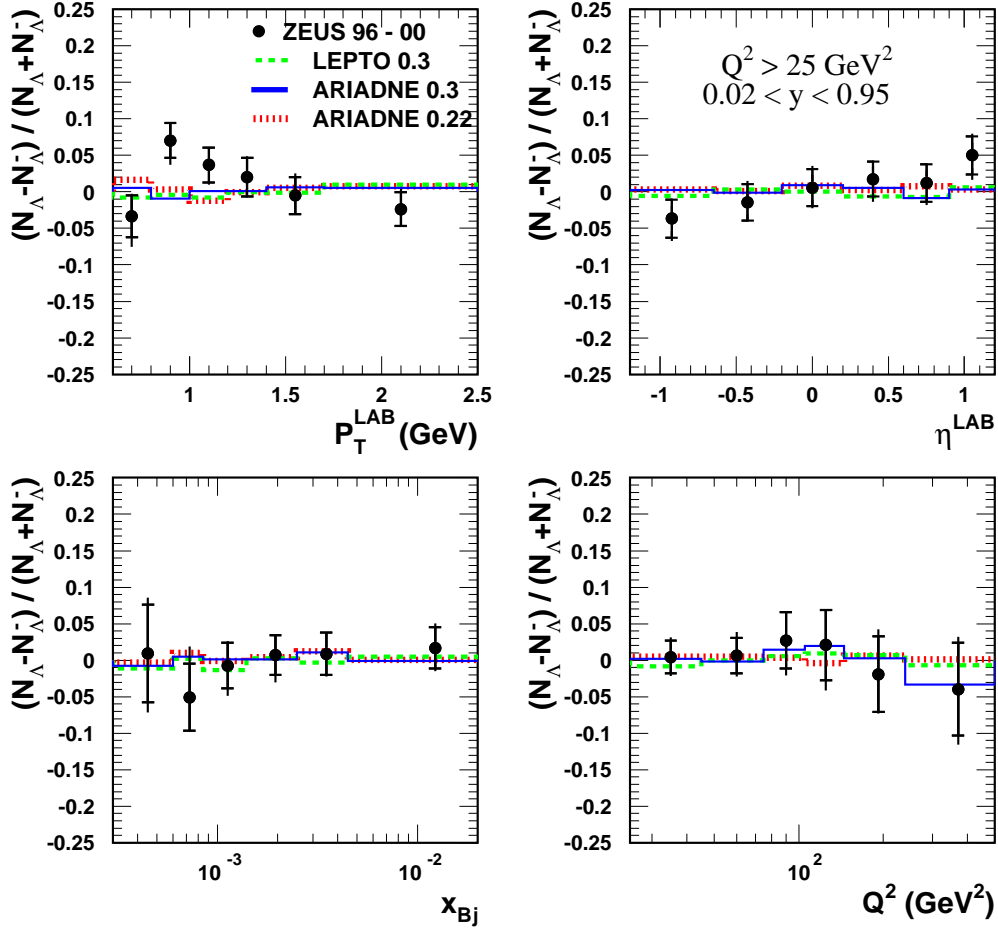


Figure 9: The ratio $\frac{N(\Lambda) - N(\bar{\Lambda})}{N(\Lambda) + N(\bar{\Lambda})}$ as a function of P_T^{LAB} , η^{LAB} , x_{Bj} and Q^2 , in the range $0.6 < P_T^{\text{LAB}} < 2.5 \text{ GeV}$ and $|\eta^{\text{LAB}}| < 1.2$ for events with $Q^2 > 25 \text{ GeV}^2$ and $0.02 < y < 0.95$. Statistical errors (inner error bars) and the systematic uncertainties added in quadrature are shown. The histograms show predictions from ARIADNE and LEPTO using the stated strangeness suppression.

ZEUS

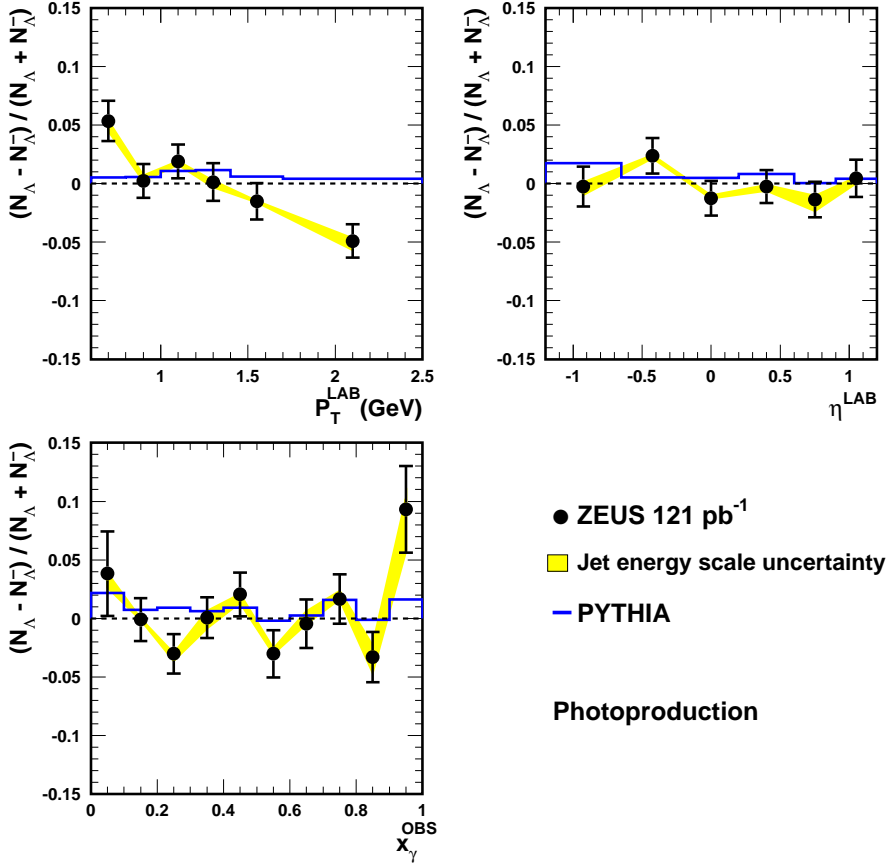


Figure 10: The ratio $\frac{N(\Delta) - N(\bar{\Delta})}{N(\Delta) + N(\bar{\Delta})}$ as a function of P_T^{LAB} , η^{LAB} and x_γ^{OBS} , in the range $0.6 < P_T^{\text{LAB}} < 2.5 \text{ GeV}$ and $|\eta^{\text{LAB}}| < 1.2$ for events with $Q^2 < 1 \text{ GeV}^2$, $0.2 < y < 0.85$ and at least two jets both satisfying $E_T^{\text{jet}} > 5 \text{ GeV}$ and $|\eta^{\text{jet}}| < 2.4$. Statistical errors are shown, together with the uncertainty arising from the jet energy scale (shaded band). The solid histogram shows the prediction from PYTHIA (with multiple interactions).

ZEUS

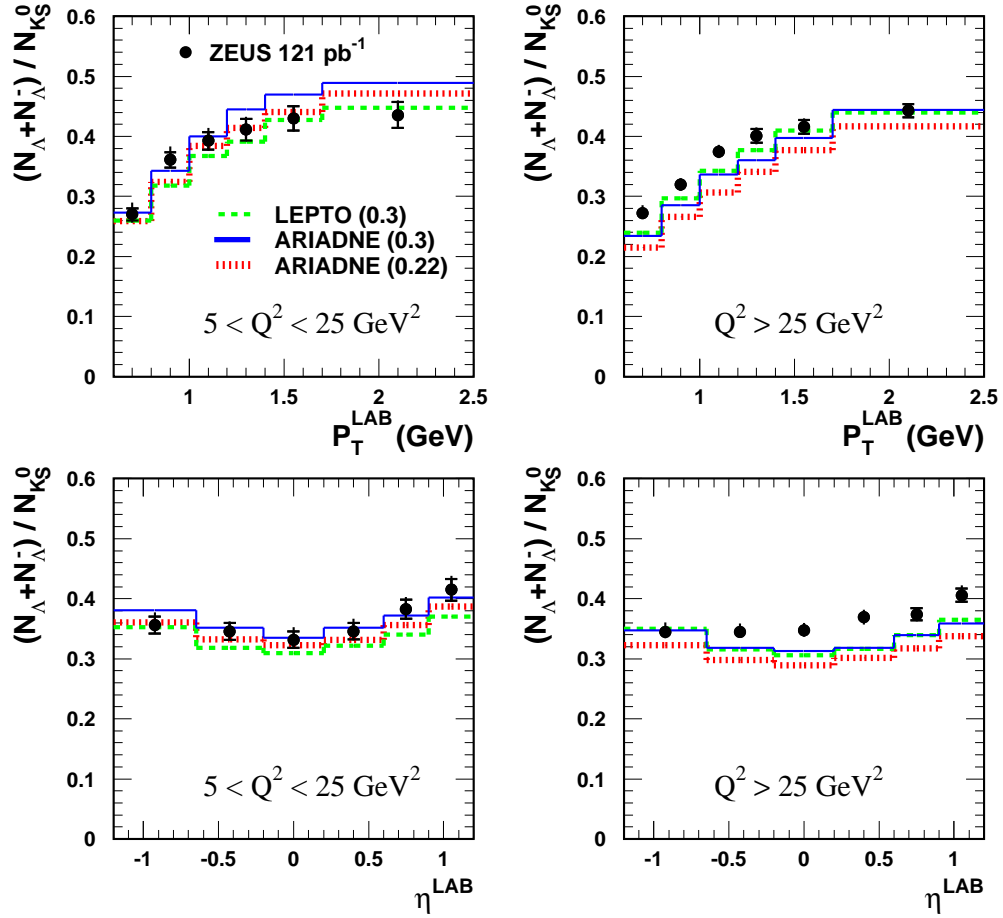


Figure 11: The ratio $\frac{N(\Lambda) + N(\bar{\Lambda})}{N(K_S^0)}$ as a function of P_T^{LAB} and η^{LAB} in the range $0.6 < P_T^{\text{LAB}} < 2.5 \text{ GeV}$ and $|\eta^{\text{LAB}}| < 1.2$ for events with $5 < Q^2 < 25 \text{ GeV}^2$, $0.02 < y < 0.95$ and $Q^2 > 25 \text{ GeV}^2$, $0.02 < y < 0.95$. Statistical errors (inner error bars) and the systematic uncertainties added in quadrature are shown. The histograms show predictions from ARIADNE and LEPTO using the stated strangeness suppression.

ZEUS

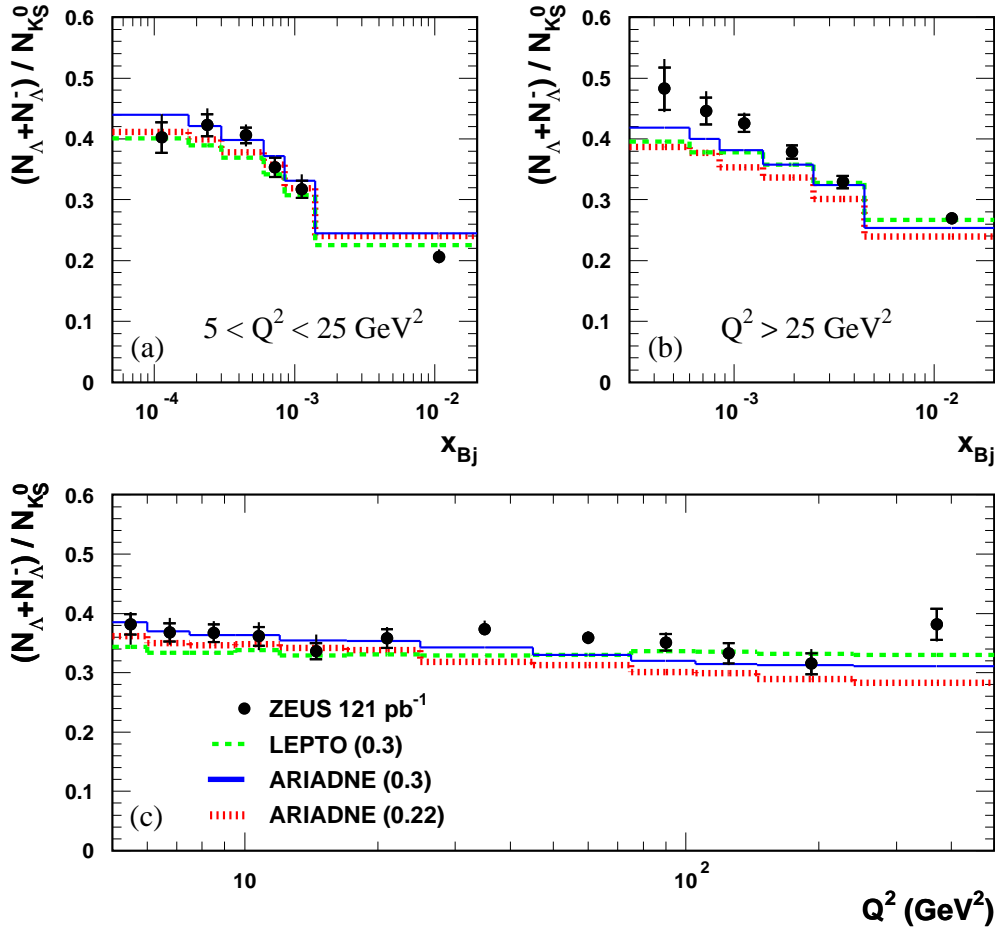


Figure 12: The ratio $\frac{N(\Lambda)+N(\bar{\Lambda})}{N(K_S^0)}$ as a function of x_{Bj} and Q^2 in the range $0.6 < P_T^{\text{LAB}} < 2.5 \text{ GeV}$ and $|\eta^{\text{LAB}}| < 1.2$ for events with a) $5 < Q^2 < 25 \text{ GeV}^2$, $0.02 < y < 0.95$ b) $Q^2 > 25 \text{ GeV}^2$, $0.02 < y < 0.95$ and c) $Q^2 > 5 \text{ GeV}^2$, $0.02 < y < 0.95$. Statistical errors (inner error bars) and the systematic uncertainties added in quadrature are shown. The histograms show predictions from ARIADNE and LEPTO using the stated strangeness suppression.

ZEUS

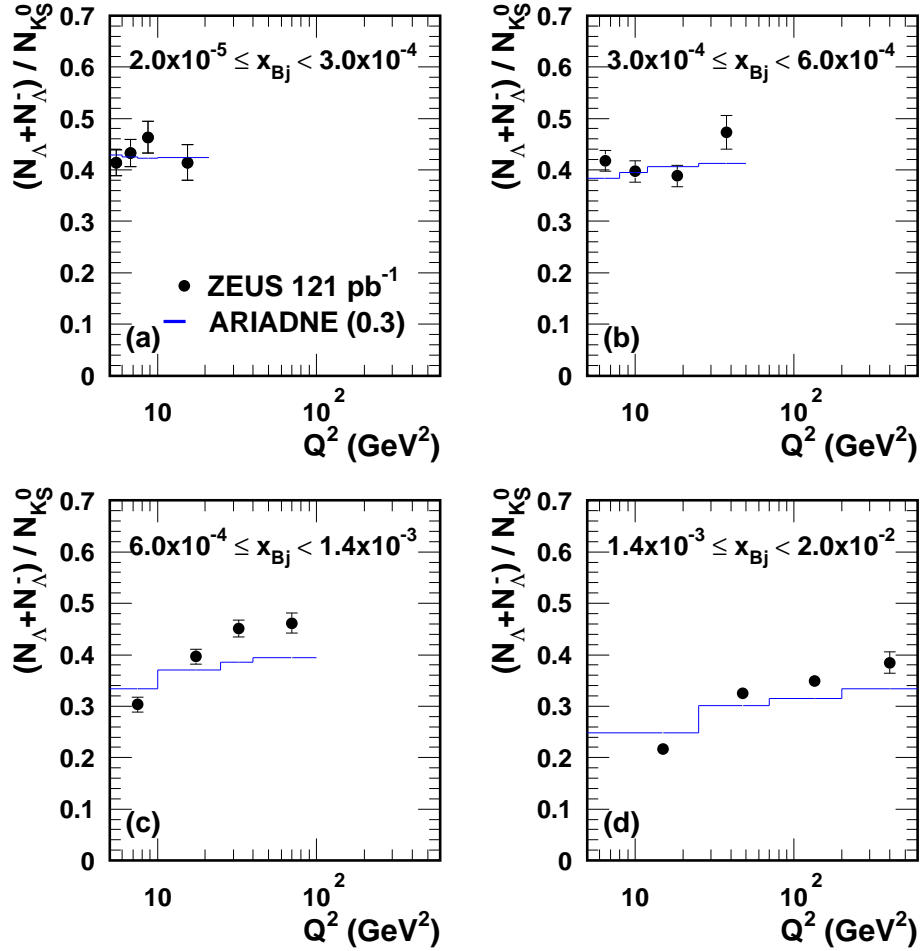


Figure 13: The ratio $\frac{N(\Lambda)+N(\bar{\Lambda})}{N(K_S^0)}$ as a function of Q^2 for four bins of x_{Bj} , in the range $0.6 < P_T^{\text{LAB}} < 2.5 \text{ GeV}$ and $|\eta^{\text{LAB}}| < 1.2$ for events with $Q^2 > 5 \text{ GeV}^2$ and $0.02 < y < 0.95$. Statistical errors only are shown. The histograms show predictions from ARIADNE with a strangeness-suppression factor of 0.3.

ZEUS

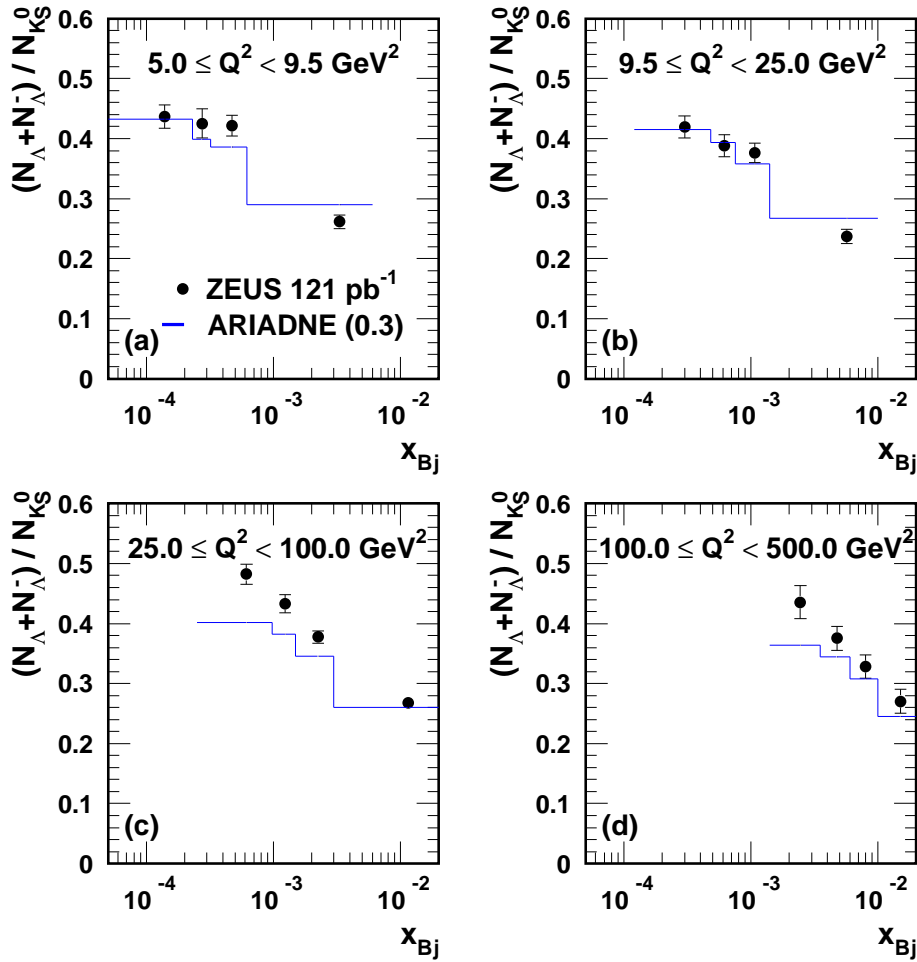


Figure 14: The ratio $\frac{N(\Lambda)+N(\bar{\Lambda})}{N(K_S^0)}$ as a function of x_{Bj} for four bins of Q^2 , in the range $0.6 < P_T^{\text{LAB}} < 2.5 \text{ GeV}$ and $|\eta^{\text{LAB}}| < 1.2$ for events with $Q^2 > 5 \text{ GeV}^2$ and $0.02 < y < 0.95$. Statistical errors only are shown. The histograms show predictions from ARIADNE with a strangeness-suppression factor of 0.3.

ZEUS

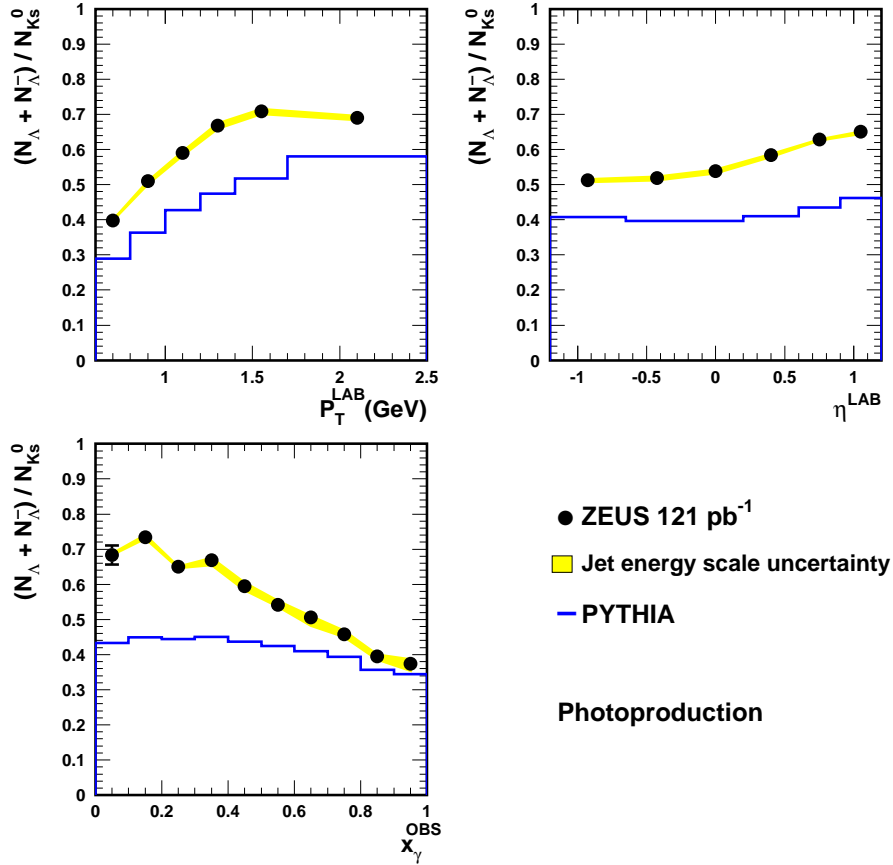


Figure 15: The ratio $\frac{N(\Delta)+N(\bar{\Delta})}{N(K_S^0)}$ as a function of P_T^{LAB} , η^{LAB} and x_γ^{OBS} , in the range $0.6 < P_T^{\text{LAB}} < 2.5 \text{ GeV}$ and $|\eta^{\text{LAB}}| < 1.2$ for events with $Q^2 < 1 \text{ GeV}^2$, $0.2 < y < 0.85$ and at least two jets both satisfying $E_T^{\text{jet}} > 5 \text{ GeV}$ and $|\eta^{\text{jet}}| < 2.4$. The statistical errors are shown, unless smaller than the point size. The shaded band shows the uncertainty arising from the jet energy scale. The solid histogram shows the prediction from PYTHIA (with multiple interactions).

ZEUS

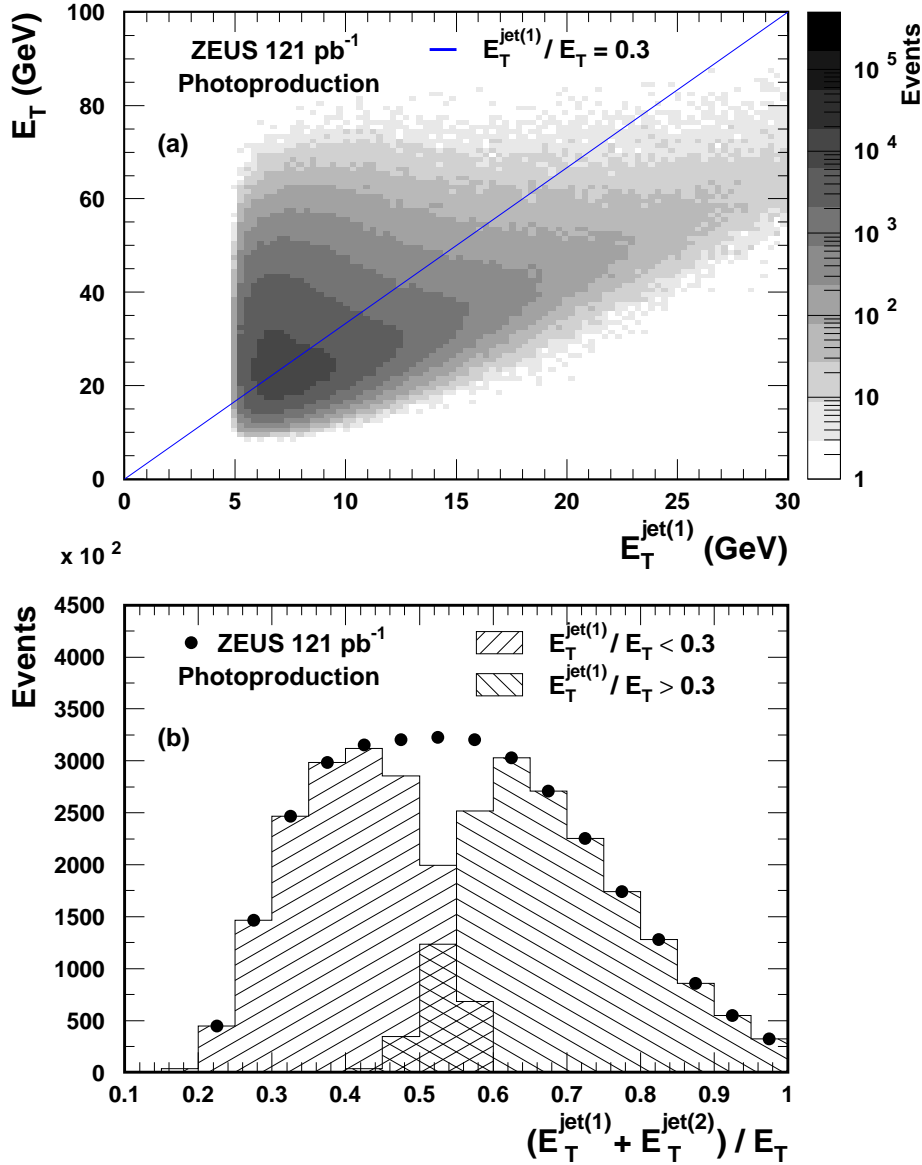


Figure 16: (a) Distribution of photoproduction events as a function of the total transverse energy and the transverse energy of the jet with the highest transverse energy. Here the event sample was selected without any strange hadron requirements. The solid line represents the cut used to separate fireball-enriched and fireball-depleted subsamples. (b) The fraction of the total E_T carried by the two jets of highest transverse energy for the same data sample as in (a). Fireball-enriched ($E_T^{\text{jet}(1)} / E_T < 0.3$) and fireball-depleted ($E_T^{\text{jet}(1)} / E_T > 0.3$) samples are shown. Statistical errors are smaller than the point size.

ZEUS

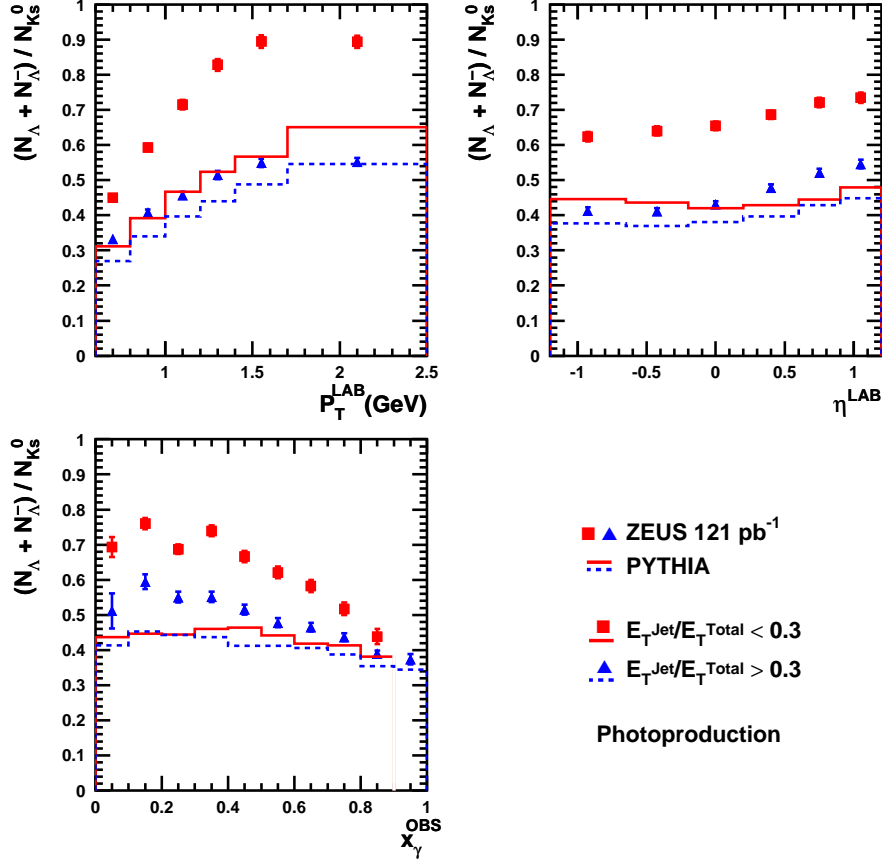


Figure 17: The ratio $\frac{N(\Lambda)+N(\bar{\Lambda})}{N(K_S^0)}$ as a function of P_T^{LAB} , η^{LAB} and x_γ^{OBS} , in the range $0.6 < P_T^{\text{LAB}} < 2.5$ GeV and $|\eta^{\text{LAB}}| < 1.2$ for events with $Q^2 < 1$ GeV², $0.2 < y < 0.85$ and at least two jets both satisfying $E_T^{\text{jet}} > 5$ GeV and $|\eta^{\text{jet}}| < 2.4$. The ratios from the fireball-enriched sample (squares) and the fireball-depleted sample (triangles) are shown for the data. The prediction from PYTHIA for the fireball-enriched (solid line) and for the fireball-depleted (dashed line) samples are shown. Statistical errors are shown. The highest x_γ^{OBS} bin ($0.9 < x_\gamma^{\text{OBS}} < 1.0$) of the fireball enriched sample is omitted due to insufficient statistics.

ZEUS

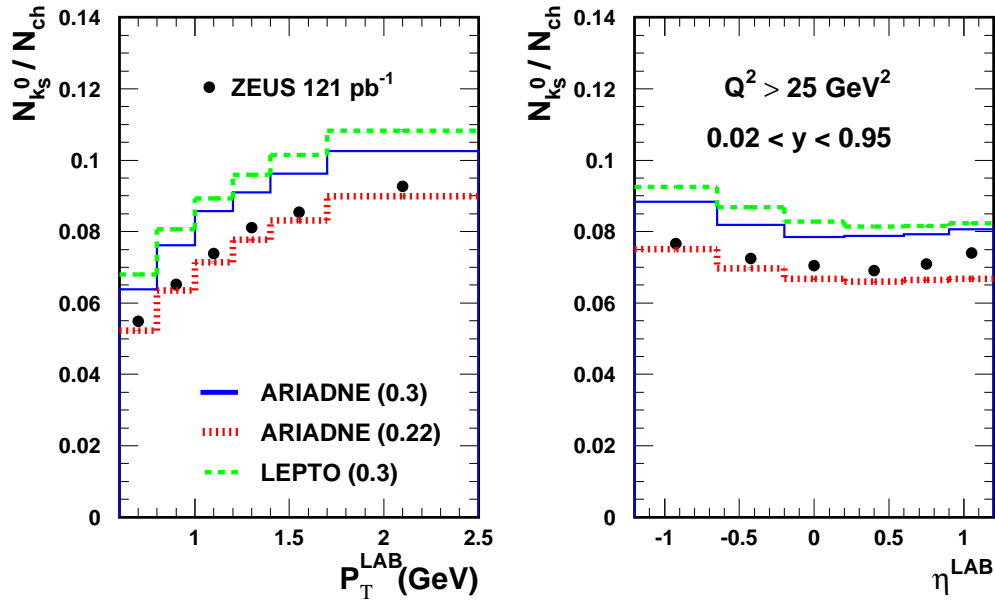


Figure 18: The ratio $\frac{N(K_S^0)}{N_{ch}}$ as a function of P_T^{LAB} and η^{LAB} , in the range $0.6 < P_T^{LAB} < 2.5 \text{ GeV}$ and $|\eta^{LAB}| < 1.2$ for events with $Q^2 > 25 \text{ GeV}^2$ and $0.02 < y < 0.95$. Statistical errors are smaller than the point size. The histograms show predictions from ARIADNE and LEPTO using the stated strangeness suppression.

ZEUS

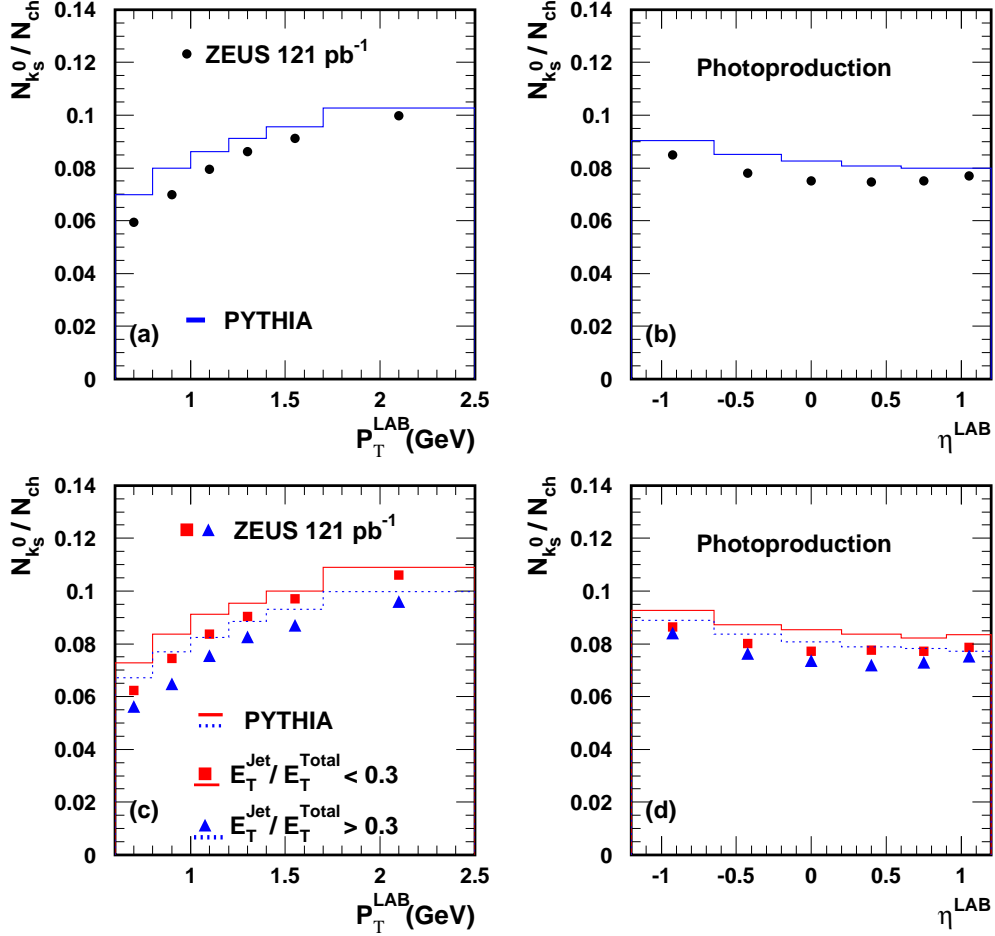


Figure 19: The ratio $\frac{N(K_S^0)}{N_{ch}}$ as a function of P_T^{LAB} and η^{LAB} , in the range $0.6 < P_T^{LAB} < 2.5 \text{ GeV}$ and $|\eta^{LAB}| < 1.2$ for events with $Q^2 < 1 \text{ GeV}^2$, $0.2 < y < 0.85$ and at least two jets both satisfying $E_T^{jet} > 5 \text{ GeV}$ and $|\eta^{jet}| < 2.4$. The ratio is shown for all events in (a) and (b) and for the fireball-enriched sample and the fireball-depleted sample in (c) and (d). Prediction from PYTHIA (with multiple interactions) predictions with a strangeness suppression factor of 0.3 are shown as solid and dashed histograms. Statistical errors are smaller than the symbols.

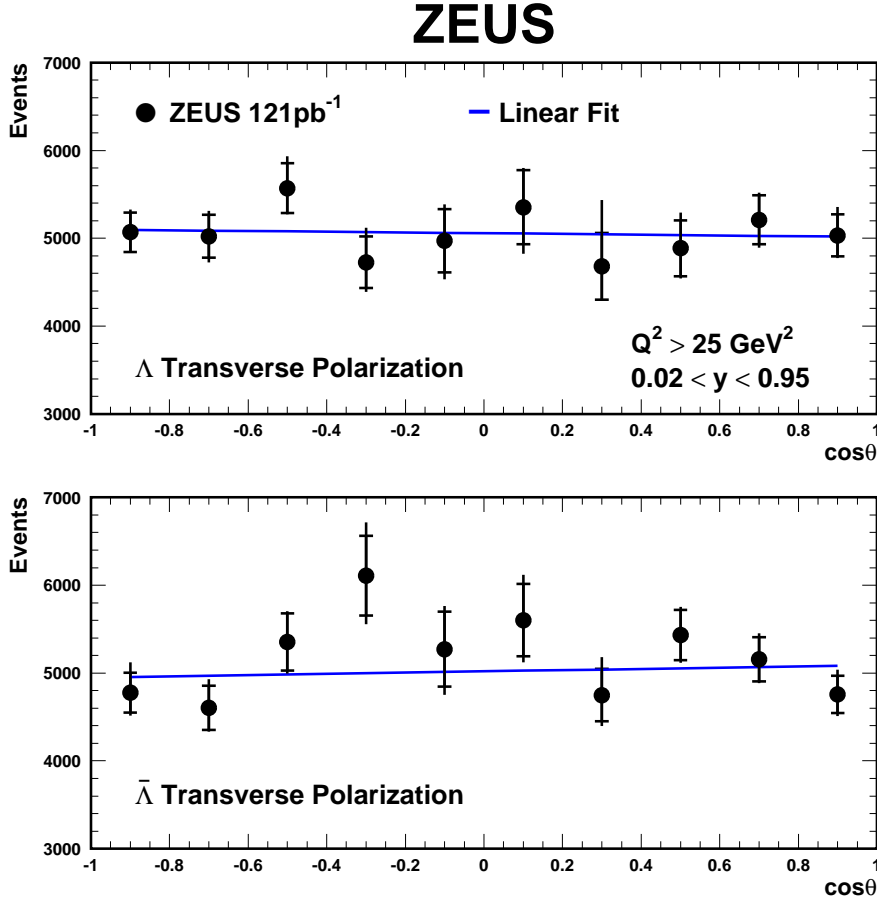


Figure 20: Angular distributions of the highest-momentum decay particle from a Λ or $\bar{\Lambda}$ in the range $0.6 < P_T^{\text{LAB}} < 2.5 \text{ GeV}$ and $|\eta^{\text{LAB}}| < 1.2$ for events with $Q^2 > 25 \text{ GeV}^2$ and $0.02 < y < 0.95$, where θ is the angle between the decay-particle momentum vector and the polarization axis, in the rest frame of the Λ or $\bar{\Lambda}$. Statistical errors (inner error bars) and the systematic uncertainties added in quadrature are shown. The first-order polynomial fit (solid line) from which the polarization is obtained is also shown.